Rock Mechanics and Rock Engineering
https://doi.org/10.1007/s00603-025-05157-5

ORIGINAL PAPER

Role of Stress Perturbations on Fault Stability During CO_2 Storage in Fractured Shale Reservoirs

Mengke An[1,2] · Rui Huang[3] · Zhen-Yu Yin[1] · Ke Gao[4] · Derek Elsworth[2,5]

Received: 18 March 2025 / Accepted: 22 November 2025

Abstract

Storing captured CO_2 in fractured shale reservoirs is a promising and feasible approach to ensure large-scale carbon reduction and realize the dual goals of carbon neutrality and environmental protection. However, increased fluid pressures and decreased effective stress may promote fault/fracture reactivation and the potential to trigger seismicity. As a typical example, we use fractured Longmaxi shale reservoirs in the southeastern Sichuan Basin to explore fluid pressure perturbations on the potential for hazardous seismicity. We conduct double-direct shear experiments on simulated Longmaxi shale gouges to explore the effects of over pressurization. Specifically, we isolate the impacts of fluid pressure reduction rates, magnitudes of initial confined stress and shear velocity, and shale mineralogy on fault peak shear velocity and durations to nucleation. A larger fault peak shear velocity and a shorter nucleation duration are proxies to indicate that the fault may be more readily reactivated. Results identify the pressure reduction rate as one of the most important external factor influencing the fault reactivation style. Elevating the pressure reduction rate apparently increases peak shear velocity to approach the dynamic fault slip rate (mm/s) for earthquake triggering and reduces the duration of nucleation. Lowering the initial confining stress and shear velocity produces similar effects. For Longmaxi shales, elevating the tectosilicate content significantly increases the peak shear velocity and nucleation duration, while elevating carbonate content shows the opposite effect. Results imply that the peak shear velocity of most shale faults should be below a threshold for earthquake triggering and highlight the importance of fault aseismic fault slip in triggering the potential for seismicity during CO_2 storage in fractured shale reservoirs.

Highlights

- Storing CO_2 in fractured shale reservoirs in Longmaxi shale is viable but may promote fault instability.
- Increasing normal stress reduction rates and lowering the confining stresses promote fault nucleation.
- Mineralogy is a single most important intrinsic factor controlling shale fault stability, especially tectosilicates and carbonates.

Keywords Carbon storage · Fractured shale reservoirs · Fault stability · Fluid overpressures · Effective stress perturbations · Nucleation velocity/duration

✉ Zhen-Yu Yin
zhenyu.yin@polyu.edu.hk

✉ Ke Gao
gaok@sustech.edu.cn

[1] Department of Civil and Environmental Engineering, The Hong Kong Polytechnic University, Hung Hom, Kowloon 100872, Hong Kong, China

[2] Department of Energy and Mineral Engineering, EMS Energy Institute and G3 Center, The Pennsylvania State University, University Park, PA 16802, USA

[3] Department of Geotechnical Engineering, College of Civil Engineering, Tongji University, Shanghai 200092, China

[4] Department of Earth and Space Sciences, Southern University of Science and Technology, Shenzhen 518055, Guangdong, China

[5] Department of Geosciences, The Pennsylvania State University, University Park, PA 16802, USA

Published online: 08 December 2025

1 Introduction

Carbon capture, utilization and/or storage (CCUS) potentially serve the increasing global demand for large-scale carbon reduction in the atmosphere and in achieving the goal of net zero greenhouse gas emissions (Rogelj et al. 2015; Zhang et al. 2020; Chen et al. 2022). This technology involves the injection of the captured CO_2 from human industrial activities into the subsurface at depths of hundreds to thousands of meters (Al Hameli et al. 2022; Bashir et al. 2024). Promising sites targeted for carbon sequestration include unmineable coalbeds, deep saline caverns or aquifers, reactive basaltic formations and depleted oil/gas reservoirs (Matter et al. 2009; Pan et al. 2016; Baabbad et al. 2022).

Currently, storing captured CO_2 in fractured shale reservoirs has proven to be a potentially effective approach (Busch et al. 2008; Furukawa And Yaghi 2009; Bui et al. 2018; Hou et al. 2024). This approach shows numerous benefits over commercial/pilot-scale CO_2 storage sites in porous oil reservoirs containing a connected pore network contributing to a highly permeable rock matrix (Fig. 1a, b) (Zoback 2007; Nelson 2009; Zivar et al. 2021; Kuang et al. 2023). First, hydraulic fracturing for shale gas recovery creates a fracture network that allows the penetration of CO_2 into the hydraulic fractures and leaves the fracture system to dominate the storage capacity (Loucks et al. 2012; Mohagheghian et al. 2019; Wang et al. 2020). Second, CO_2 has a greatly enhanced adsorptive affinity to the carbon-rich reservoir rocks than CH_4 (~ 5:1)—preferentially fixing the adsorption-trapped CO_2 in the abundant nano-pores of the tight shale matrix (Eshkalak et al. 2014; Boosari et al. 2015). Finally, the extremely low (nanoscale) permeability of the rock matrix in organic-rich reservoir shales promotes sealing and constrains fugitive gas migration, thus ensuring the intrinsic safety of CO_2 storage (Ambrose et al. 2008; Gale et al. 2014; Edwards et al. 2015). In addition, it is possible to integrate the use of CO_2 as the fracturing fluid to increase oil/gas production while maintaining the potential of CO_2 storage, realizing a win–win situation for carbon neutrality and enhanced oil/gas recovery (Louk et al. 2017; Gan et al. 2021; Han et al. 2024).

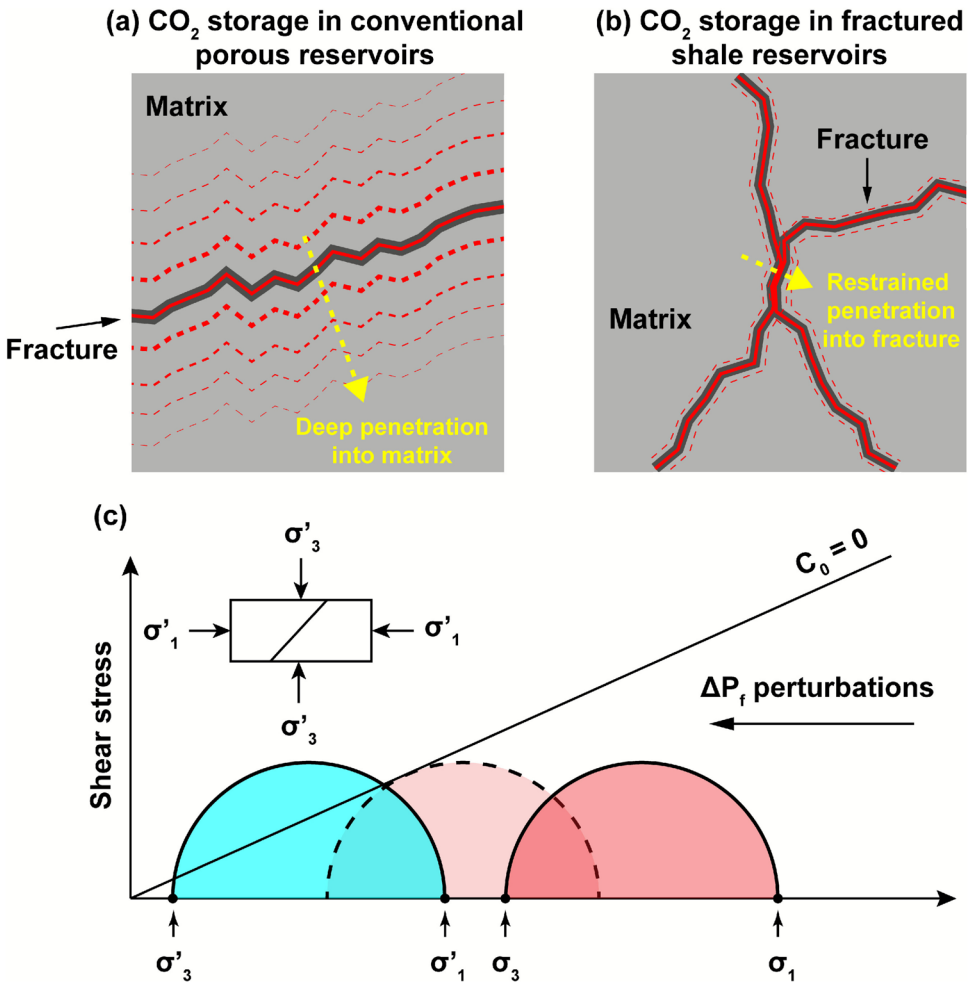

Fig. 1 Comparison of CO_2 storage mechanisms in **a** conventional porous reservoirs and **b** fractured shale reservoirs, adapted from Hou et al. (2024). **c** The evolution of the stress state with increasing pore fluid pressure as a result of CO_2 injection is indicated by the Mohr circle plot. Symbols σ_1 and σ_1' represent the maximum principal stress, and symbols σ_3 and σ_3' represent the minimum principal stress

However, CO_2 sequestration in fractured shales also poses risks of deep fault reactivation and induced seismicity (Cappa And Rutqvist 2011; Vilarrasa et al. 2016, 2019; Yin et al. 2025; Zhang et al. 2024). Factors influencing fault stability include the selected CO_2 injection strategies (e.g., the injection rate, volume, and duration), in-situ tectonic environment (e.g., the thermal gradient, tectonic stress, geologic structure, and chemical fluids) and fault characteristics (e.g., the location, geometry, structure, mineralogy, and permeability) (Frohlich et al. 2016; Foulger et al. 2018; Moein et al. 2023). There are five possible mechanisms for fault instability induced by the direct injection of CO_2 into the fractured shale reservoirs (Vilarrasa et al. 2019). First, the injection of CO_2 could increase pore fluid pressures and thereby decrease effective stress on transected or adjacent faults, enabling fault reactivation in shear (Bao And Eaton 2016; Elsworth et al. 2016). However, unlike water injection, yielding a linear increase in pore pressure with the logarithm of time (continuous fluid injection), CO_2 injection potentially yields a stable long-term overpressure after reaching a peak during initial injection (Henninges et al. 2011; Vilarrasa et al. 2013). Second, the non-isothermal effects of injecting a cold fluid into a hot reservoir potentially induce thermal stresses and local stress redistribution within the quenched region and may thereby affect fault stability (Jeanne et al. 2014). Third, when low-permeability faults transect the injection region, the resulting steep pressure gradients may possibly promote fault instability (Faulkner et al. 2006). Fourth, poroelastic stress transfer from CO_2 injection may project distant fault loading and lead to fault reactivation on critically stressed faults—even absent a direct hydraulic connection (Ellsworth et al. 2013; Segall And Lu 2015). In addition, aseismic slip within the pressurized region may load and reactivate distant faults with this stress transfer potentially triggering seismicity (Eyre et al. 2019). Finally, the dissolution of CO_2 into the subsurface fluids will form acidic solutions, with this solution potentially dissolving minerals such as clays, carbonates (calcite, dolomite, magnesite), feldspars (plagioclase and microcline) and augite. Changes in fault zone porosity and permeability may impact the stability of pre-existing fractures/faults (Alam et al. 2014; An et al. 2020a).

The elevation of pore pressures is the most direct and predominant mechanism driving fault instability under successive fluid injection conditions (Ellsworth et al. 2013; Moein et al. 2023). Here, we focus on the effect of such successive injections of CO_2 on fault stability in shales and then analyze the potential for shear failure on pre-existing fluid-pressurized fractures/faults. Shear reactivation can be described by the Coulomb failure criterion. That is, failure of a fault will occur when the shear stress τ acting on the fault plane exceeds the shear strength τ_s:

$$\tau - \tau_s = \tau - \left(C_0 + \mu_s \bullet \sigma_{neff}\right) \geq 0 \quad (1)$$

where C_0 is the cohesion (usually equal to 0 for pre-existing and active faults due to the granular fault gouge particles within the faults), μ_s is the static frictional coefficient of the fault, and σ_{neff} is the effective normal stress applied on the fault plane. Coulomb failure stress (ΔCFS) can be used to evaluate whether a fault is approaching or retreating from failure. This may be defined as a function of normal and shear stress as (King et al. 1994; Hill 2008)

$$\Delta CFS = \Delta\tau - \mu_s \bullet \left(\Delta\sigma_n - \Delta P_f\right) = \Delta\tau - \mu_s \bullet \Delta\sigma_{neff} \quad (2)$$

where $\Delta\tau$, $\Delta\sigma_n$, ΔP_f, and $\Delta\sigma_{neff}$ represent changes in shear stress, normal stress, pore fluid pressure and effective normal stress, respectively. Successive stages of CO_2 injection potentially induce perturbations in stress on the pressurized fault with changes in the Coulomb failure stress (ΔCFS) serving as a harbinger for fault reactivation (Fig. 1c). We use the fractured gas shale reservoirs of the Sichuan Basin of southwest China as characteristic of other similar reservoirs and perform shear reactivation experiments to explore the impact of CO_2 injection-induced stress perturbations on the evolution of fault failure.

2 Experimental Methods

2.1 Shale Gouge Preparation

We use shales from the lower Silurian Longmaxi formation recovered from the Lijiawan Quarry, Yanjin County, Zhaotong City, Yunnan Province, southwest China (Fig. 2a). The geographic coordinates of the quarry are 104°26′33.9″ E and 28°07′55.4″ N with more details on characteristics provided in An et al. (2020b). These shales are currently the most important target for shale gas recovery in the Sichuan Basin, southwest China. The Longmaxi shales outcropping in the Lijiawan Quarry were deposited in the same geological period as the deep shales of Changning, Weiyuan, and Luzhou—important national shale gas demonstration blocks (Fig. 2b). The Lijiawan shales are exposed at the surface as a result of multiple polycyclic tectonic movements (Guo 2013; Tan et al. 2014), although, otherwise, are fully representative of the deep reservoir shales of the Longmaxi formation of the southeastern Sichuan Basin.

We recovered a total of 32 shale samples (sample numbers Shale_5 to Shale_38) from the geologic section in Lijiawan Quarry to represent the full stratigraphic sequence of the Longmaxi Formation shales (Fig. 2c). X-ray diffraction (XRD) was employed to determine mineral compositions at the Micro Structure Analytic Laboratory of Peking University, Beijing, China, using a Rigaku D/max-rB X-ray

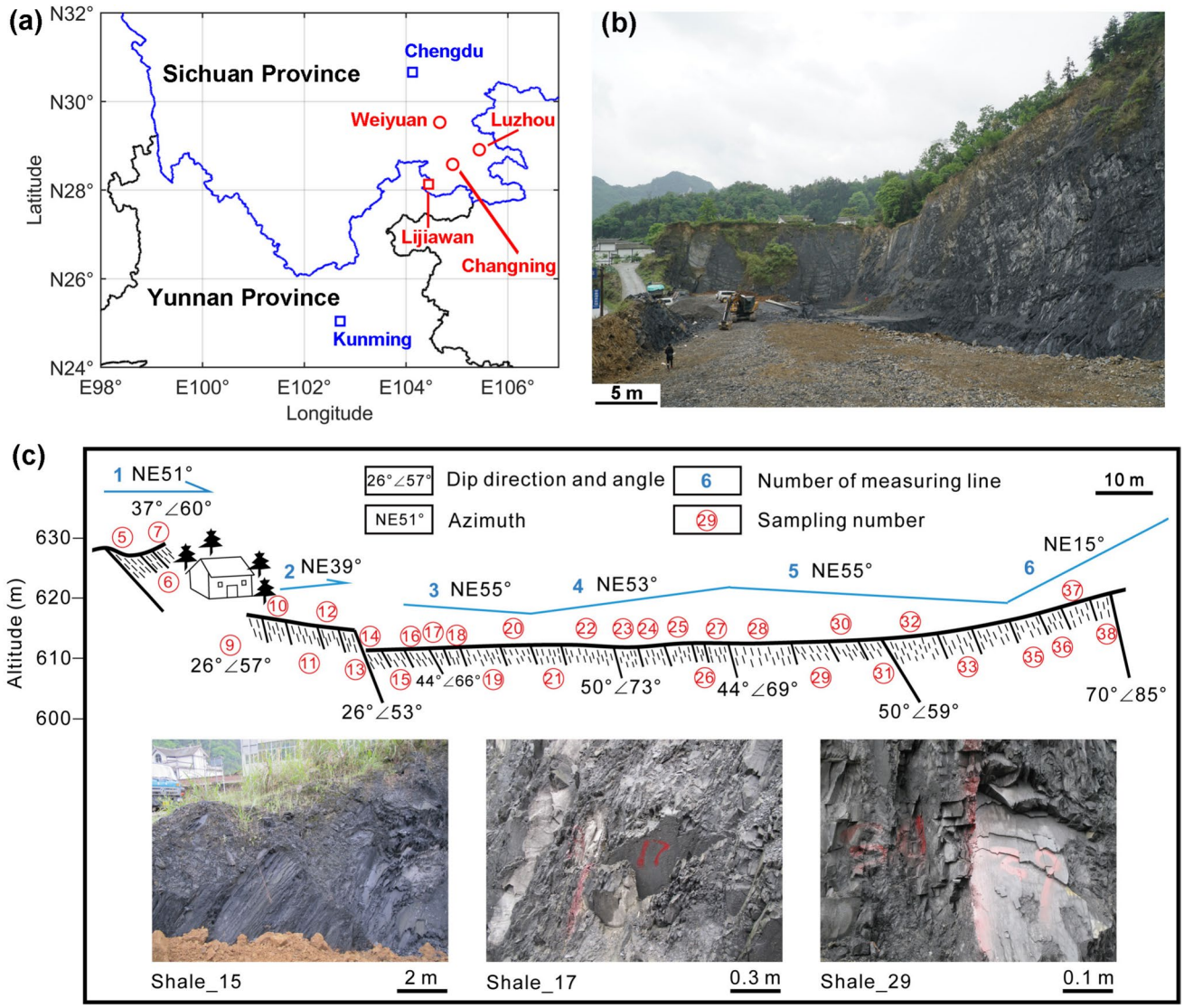

Fig. 2 **a** Locations of the Lijiawan Quarry (red square) and Changning, Weiyuan, and Luzhou areas (red circles) in the southeastern Sichuan Basin. The blue and black lines denote the boundaries of Sichuan and Yunnan Provinces, respectively. Blue squares indicate Chengdu and Kunming cities, respectively. **b** The exposed Longmaxi formation shales in the Lijiawan Quarry face. **c** A schematic showing the geologic section and shale sampling locations (Shale_5 to Shale_38) in the Lijiawan Quarry together with photos of three representative shale sampling locations (Shale_15, Shale_17, and Shale_29). Shale samples and related sampling location numbers increase from the base to the top of the stratigraphic section. Shale_8 is buried under a house and shale_34 is buried by a thick layer of bentonite. Thus, these two shales were difficult to recover and not sampled

diffractometer—with detailed results reported in An et al. (2020b). Results identify the Longmaxi shales as primarily comprising quartz, feldspar, clay minerals (mostly illite and chlorite), calcite, dolomite and traces of pyrite. We further classify these component minerals into groups as tectosilicates, phyllosilicates and carbonates based on their similar crystal structures and frictional properties and following the practice of Fang et al. (2018) and Kohli and Zoback (2013). The tectosilicates primarily include quartz and feldspar, the phyllosilicates primarily clay minerals and with calcite and dolomite dominating the carbonates. The tectosilicates show a structure with four oxygen atoms of SiO_4 tetrahedra shared by other tetrahedra (Fang et al. 2018). This crystal structure promotes high hardness and thus high frictional strength and velocity-weakening (potentially unstable slip) response. The carbonates have a rhombohedral structure and they also exhibit high frictional strength. Conversely, the layered structures in phyllosilicates are less resistant to shear and generally show low frictional strength and velocity-strengthening (stable slip) response. The tectosilicate content decreases from the base to the top of the stratigraphic section (i.e., with increasing sampling numbers), while the

carbonate content shows the opposite trend. Phyllosilicate contents are primarily in the range 20–40 wt.% and change uniformly over the section. The mineralogical transition from tectosilicate-dominated to carbonate-dominated shales is common in Longmaxi shales with this phenomenon primarily attributed to the sedimentary environments changing from intra-shelf to shallow shelf during sedimentation (Xu et al. 2019).

We select eight samples (sampling numbers: Shale_7, Shale_11, Shale_15, Shale_17, Shale_26, Shale_29, Shale_35 and Shale_38) as representative of these mineralogical trends from the 32 collected shale samples to conduct the fault gouge shear reactivation experiments. The mineral compositions of the eight shales are shown in Table 1, with the tectosilicate, phyllosilicate and carbonate contents spanning the ranges 14–76 wt.%, 6–38 wt.%, and 0–80 wt.%. The variations in tectosilicate or carbonate contents in these eight selected shales reflect the mineralogical heterogeneity over the entire Longmaxi stratigraphic section. After removing surface impurities, the shales were crushed and sieved to particle diameters < 106 μm to represent fault gouge. The powdered shales do not fully represent the in-situ fault gouge materials as fault shear offsets can be large and contrasting lithologies are present in opposite walls of the contacting fault, broadening the mineralogical distribution. However, they are the best representation of the fault gouge as the fault gouge is primarily a wear product from the fault wall/surrounding rock. The particle size distributions comprising D10, D50 and D90 (particle diameter passing 10, 50 and 90 vol.%) are shown in Fig. 3 and Table 2. Values of D10, D50, and D90 of these shale powders are primarily within the ranges 0.7–1.5, 4.1–12.8 and 24.1–96.3 μm, respectively, with values of D90 in Shale_7, Shale_15, and Shale_29 much lower than in the other shales. The Longmaxi shales include carbonaceous, calcareous, siliceous and argillaceous shales and mineralogical contents varying from top to base in the formation. This change in mineralogy would also affect the difference in particle diameters between the simulated shale gouges even if they are crushed and ground under the same conditions.

2.2 Experimental Apparatus

Our shear experiments were completed on fault gouge using the double-direct shear apparatus (Fig. 4a) developed in the Department of Earth and Space Sciences, Southern University of Science and Technology, Shenzhen, China. This apparatus comprises four components, i.e., the control and loading systems, the double-direct shear assembly and the data acquisition system. The control system comprises two high-performance computers that may separately set experimental parameters and control the entire testing process. The apparatus may run under pre-defined load, displacement, or shear velocity control modes. The loading system independently or simultaneously applies horizontal and vertical loads via the two loading pistons transiting the load frame on the upper and right sides. Both horizontal and vertical loads are applied during the tests via the servo-controlled hydraulic pumps. The maximum designed horizontal and vertical loading capacities of the piston are 1000 kN to a precision of ± 0.5 kN. The data sampling system includes two high-precision linear variable differential transducers (LVDT). Two load cells are attached to the loading pistons and measure the horizontal and vertical loads to a precision of ± 1 N.

Table 1 Mineral compositions (in weight percentage *wt.%*) of the eight selected shales

Shale samples	Shale_7	Shale_11	Shale_15	Shale_17	Shale_26	Shale_29	Shale_35	Shale_38
Quartz	68.0	46.0	35.0	32.0	24.0	22.0	18.0	4.0
Albite	5.0	14.0	17.0	13.0	8.0	8.0	6.0	6.0
Orthoclase	3.0	6.0	4.0	7.0	3.0	5.0	2.0	3.0
Pyrite	–	–	6.0	2.0	2.0	2.0	–	1.0
Illite	22.3	30.3	8.4	15.5	23.6	17.3	18.3	3.7
Chlorite	0.3	–	8.1	10.8	9.1	10.0	1.5	1.1
Kaolinite	–	–	2.1	–	–	–	–	–
I/S	1.4	–	0.4	4.7	5.3	3.7	–	1.2
C/S	–	3.7	–	–	–	–	2.2	–
Calcite	–	–	10.0	11.0	22.0	29.0	52.0	80.0
Dolomite	–	–	9.0	4.0	3.0	3.0	–	–
Tectosilicates	76.0	66.0	62.0	54.0	37.0	37.0	26.0	14.0
Phyllosilicates	24.0	34.0	19.0	31.0	38.0	31.0	22.0	6.0
Carbonates	–	–	19.0	15.0	25.0	32.0	52.0	80.0

The abbreviations "I/S" and "C/S" represent the illite/smectite mixed layer and chlorite/smectite mixed layer, respectively. The symbol "×" indicates that the sample was not tested. We define tectosilicate group minerals as of quartz, albite, orthoclase and pyrite, phyllosilicates as of illite, chlorite, kaolinite, I/S and C/S, and carbonates as of calcite and dolomite

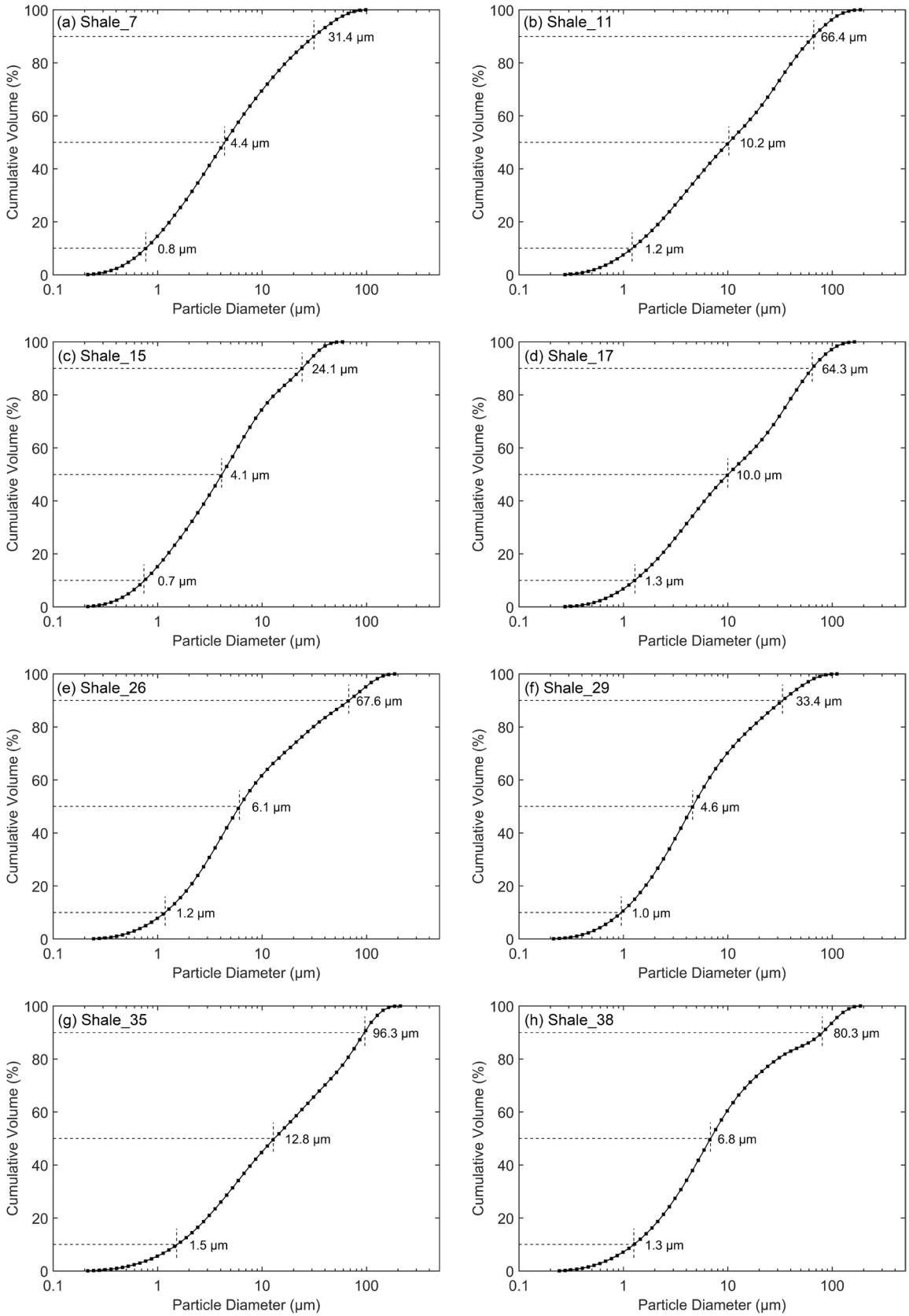

Fig. 3 Particle size (diameter) distributions of the eight collected Longmaxi shales with D10, D50 and D90 values marked, **a** Shale_7, **b** Shale_11, **c** Shale_15, **d** Shale_17, **e** Shale_26, **f** Shale_29, **g** Shale_35, and **h** Shale_38

Table 2 Particle sizes corresponding to D10, D50, and D90 of the eight selected shale gouges

Shale samples	Shale_7	Shale_11	Shale_15	Shale_17	Shale_26	Shale_29	Shale_35	Shale_38
D10 (μm)	0.8	1.2	0.7	1.3	1.2	1.0	1.5	1.3
D50 (μm)	4.4	10.2	4.1	10.0	6.1	4.6	12.8	6.8
D90 (μm)	31.4	66.4	24.1	64.3	67.6	33.4	96.3	80.3

D10, D50, and D90 denote the sizes of 10, 50, and 90 *vol.%* (volume percentage) shale particles below this diameter

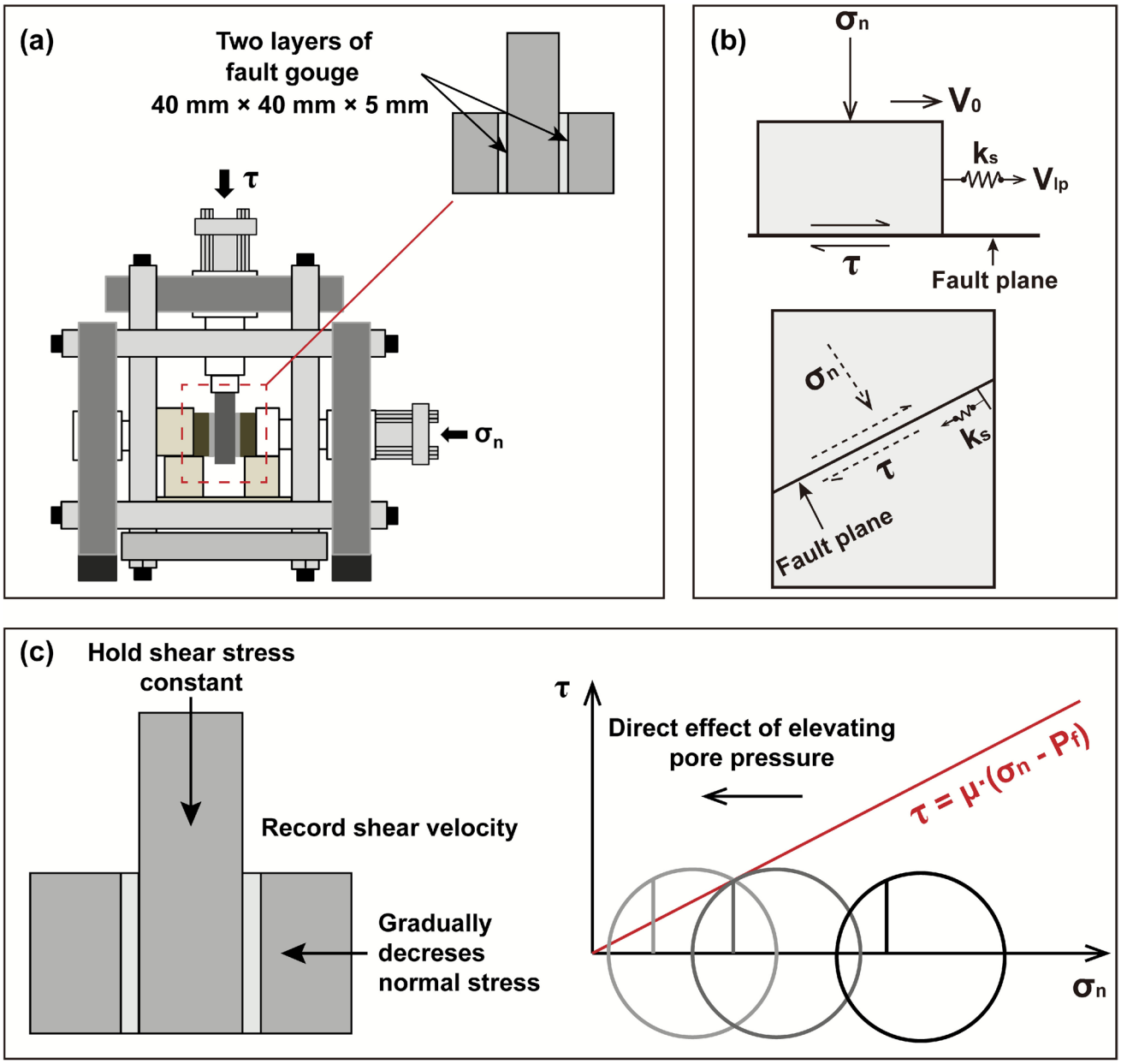

Fig. 4 **a** Schematic showing shear loading frame and the double-direct shear configuration. **b** Conceptual fault sliding model based on a single degree-of-freedom spring–slider model (Yoshida And Kato 2003). **c** Coulomb-type failure criterion illustrating the conditions for fault reactivation as a result of progressive fluid pressure elevation or effective stress decrease. Symbols σ_n, τ, P_f, μ, k_s, V_0 and V_{lp} represent the normal stress, shear stress, pore fluid pressure, fault coefficient of friction, fault stiffness coefficient, block shear velocity and load point velocity, respectively

The LVDTs are fixed to the load frames and record normal and shear displacements to a resolution of ± 0.1 µm. The load cells and displacement transducers are all calibrated by the manufacturer before the shear tests.

The fault gouge shear experiments were performed using the double-direct fault shear assembly following the methods of Mair and Marone (1999) and Ikari et al. (2009). This assembly consists of three stainless steel blocks/platens sandwiching two layers of fault gouge with the normal and shear stresses applied by the horizontal and vertical pistons, respectively (Fig. 4a). The central steel block has a dimension of 10 cm × 4 cm × 3 cm (length × width × height) and the two outer blocks measure 4 cm × 4 cm × 2 cm (length × width × height). Shear initiates by forcing the central steel block downwards while keeping the horizontal normal stress constant. Thus, these block dimensions ensure a constant contact area of 16 cm^2 throughout the entire test. The surfaces of the steel platens contain saw-teeth as dense triangular grooves (1-mm width and 0.8-mm height) with ridges perpendicular to the shear direction—to minimize boundary shear and maximize localization within the gouge layer. Fault gouge thickness for all tests was precisely controlled to be 5 mm by the use of a leveling jig. We also ensure identical masses in each of the two layers of gouge using a balance to maintain similar initial densities and porosities (Frye And Marone 2002). All experiments were conducted at room temperature (~ 20 °C) and room humidity (~ 60%). However, this humidity would have a minor effect on the experimental result as we dried the gouge before the tests and each test lasted only for a few hours.

2.3 Testing Procedures and Experimental Data

Fault frictional sliding behavior is analyzed based on a single-degree-of-freedom spring–slider model (Fig. 4b) that comprises a block (slider) and an activating spring loading the block through a pre-defined shear velocity applied to a load point (Yoshida And Kato 2003; Fukushima et al. 2023). From Amontons' law ($\tau = \mu \cdot (\sigma_n - P_f) = \mu \cdot \sigma_{neff}$), we assume that the influence of increasing the fault zone pore fluid pressure would be identical to decreasing the effective normal stress (σ_{neff}). Therefore, unlike conventional shear tests with stepped fluid pressures from successive fluid injections (Scuderi And Collettini 2018), we hold shear stress constant at steady-state friction and gradually decrease the total normal stress. We then record the evolution of shear velocity and observe how shear failure accelerates, as illustrated in Fig. 4c. This experimental design imposes similar stress perturbations to those resulting from fluid injection but on unjacketed and unconfined samples. We vary initial normal stresses, gouge mineralogy (by sample number/location), initial fault sliding velocity and effective normal stress reduction rate (equivalent to the pore fluid pressure increasing rate) and record the evolution of shear velocity as a proxy for evolving instability. We did not directly elevate the pore fluid pressure but use a gradually decreased effective normal stress to conduct the experiments, also for the following reasons. We attempted to elevate the pore fluid pressure but could not maintain steady experimental control. Thus, we choose to gradually decrease the effective normal stress as a direct proxy. Besides, some of Longmaxi shales show a high proportion of clays and finer particles and these would have an effect in achieving steady and uniformly distributed pore fluid pressure.

A total of 20 groups of experiments were conducted at varied normal stress reduction rates, initial normal stresses, shale compositions (samples) and initial shear velocities, with experiment details summarized in Table 3. A total of four suites of experiments were run to isolate and examine the individual influences of (i) normal stress reduction rate, (ii) initial normal stress, (iii) mineralogical controls, and (iv) initial shear rate on the evolution of shear velocity and to explore controls on the onset of instability. Four experiments (CHS_NR1, CHS_NR2, CHS_NR5 and CHS_NR10) were performed at a constant initial normal stress of 40 MPa, a constant initial shear velocity of 1.0 µm/s but different normal stress reduction rates from 0.01 to 0.10 MPa/s on gouge Shale_15, to define *controls of normal stress reduction rate* on fault shear velocity evolution. Another four experiments (CHS_N20, CHS_N30, CHS_N50 and CHS_N60) were conducted at a constant initial shear velocity of 1.0 µm/s, a constant normal stress reduction rate of 0.01 MPa/s but initial normal stresses of 20–60 MPa on gouge Shale_15, to explore the effect of *initial normal stress* on fault shear velocity evolution. Seven shear tests (CHS_Sh7, CHS_Sh11, CHS_Sh17, CHS_Sh26, CHS_Sh29, CHS_Sh35 and CHS_Sh38) were performed at constant initial normal stress, initial shear velocity and normal stress reduction rate but on different shale gouges, to define the *mineralogical controls* on fault shear velocity evolution. In addition, five experiments (CHS_SV0.3, CHS_SV3, CHS_SV10, CHS_SV20 and CHS_SV30) were conducted at a constant initial normal stress of 40 MPa, a constant normal stress reduction rate of 0.01 MPa/s but initial shear velocities from 0.3 to 30 µm/s, to explore the influence of *initial shear rate* on fault shear velocity evolution.

At the initiation of each shear test, the gouges were sheared at a pre-defined shear velocity (V_0) and initial normal stress (σ_n) until reaching steady-state friction at time t_0. Then, we gradually decreased the normal stress (σ_n) at a pre-defined normal stress reduction rate while keeping the shear stress (τ) constant at a shear displacement of 2–3 mm and at time t_{ini}. Finally, we record the evolution of fault shear velocity and observe the styles of slip. We repeat this for successive reactivations with the entire experimental cycle illustrated in Fig. 5. We

Table 3 Experiment matrix and details

Experiment ID	Initial normal stress (MPa)	Initial shear velocity (μm/s)	Initial shear displacement (mm)	Shale gouge	Normal stress reduction rate (MPa/s)	Peak shear velocity V_h (μm/s)	Nucleation duration $t_{nuc} - t_{ini}$ (s)
Changing the normal stress reduction rate							
CHS_NR1	40	1.0	3.0	Shale_15	0.01	299.5	113
CHS_NR2	40	1.0	3.0	Shale_15	0.02	518.1	71
CHS_NR5	40	1.0	3.0	Shale_15	0.05	1887	64
CHS_NR10	40	1.0	3.0	Shale_15	0.10	2401	34
Changing the initial normal stress							
CHS_N20	20	1.0	3.0	Shale_15	0.01	568.4	98
CHS_N30	30	1.0	3.0	Shale_15	0.01	457.4	152
CHS_N50	50	1.0	3.0	Shale_15	0.01	58.4	177
CHS_N60	60	1.0	3.0	Shale_15	0.01	84.3	232
Changing the shale gouge							
CHS_Sh7	40	1.0	3.0	Shale_7	0.01	1764	244
CHS_Sh11	40	1.0	3.0	Shale_11	0.01	636.7	228
CHS_Sh17	40	1.0	3.0	Shale_17	0.01	735.9	286
CHS_Sh26	40	1.0	3.0	Shale_26	0.01	156	219
CHS_Sh29	40	1.0	3.0	Shale_29	0.01	70.2	121
CHS_Sh35	40	1.0	3.0	Shale_35	0.01	333.4	217
CHS_Sh38	40	1.0	3.0	Shale_38	0.01	94.6	171
Changing the initial shear velocity							
CHS_SV0.3	40	0.3	2.0	Shale_15	0.01	182.7	184
CHS_SV3	40	3.0	3.0	Shale_15	0.01	397.9	134
CHS_SV10	40	10.0	3.0	Shale_15	0.01	823.6	284
CHS_SV20	40	20.0	3.0	Shale_15	0.01	170.9	216
CHS_SV30	40	30.0	3.0	Shale_15	0.01	85.1	266

The initial fault shear velocity is set as 0.3 μm/s for test CHS_SV0.3. This slow velocity would promote an early steady state and thus we shorten the shear displacement to 2.0 mm. As fault stability is also related to the evolution of gouge porosity, a different initial shear velocity would introduce a different fault gouge porosity. Hence, we also explored the impact of the initial shear velocity on fault nucleation

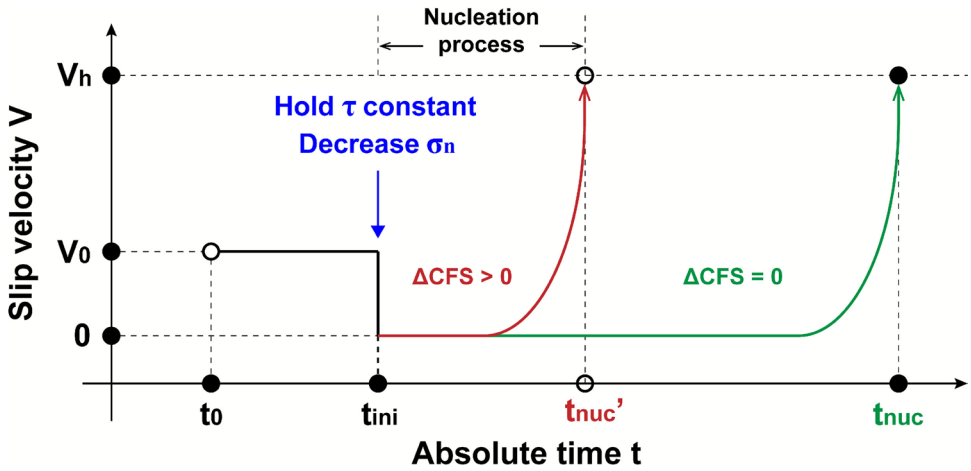

Fig. 5 Schematic showing slip velocity evolving following successive fluid injections during CO_2 storage. Symbols V_h, V_0, t_0, t_{ini}, and t_{nuc}, respectively, represent maximum shear velocity, initial shear velocity, time when steady-state friction first reached, time of normal stress reduction and time corresponding to the maximum shear velocity

define the peak shear velocity as V_h and the corresponding time as the nucleation time t_{nuc}. The duration from t_{ini} to t_{nuc} defines the duration of nucleation ($t_{nuc}-t_{ini}$). Specifically, we evaluate the impacts of changes in experimental conditions on the maximum shear velocity V_h and the duration of nucleation. According to Scuderi and Collettini (2018), instability occurs when the peak shear velocity exceeds the dynamic fault slip rate

(~ mm/s). A shorter nucleation duration indicates that the fault will be readily reactivated, and a longer nucleation duration implies an increased resistance to reactivation. Final shear displacements in individual tests over multiple cycles are < 7–8 mm with the sampling frequency set to 1 Hz.

3 Results

We evaluated the evolution of fault shear velocities resulting from (i) different rates of normal stress reduction (representing increased fluid pressure elevation rates), (ii) initial normal stresses, (iii) initial shear velocities, and (iv) mineralogy. We focus on the impacts of the above parameters on fault peak shear velocity (V_h) and the duration of nucleation time ($t_{nuc}-t_{ini}$), with a larger peak shear velocity and a shorter nucleation duration indicating greater propensity for reactivation. We also compare the magnitudes of normal stress drops ($\Delta\sigma_n$) during the fault nucleation process and ratios of normal stress drop to initial normal stress ($\Delta\sigma_n/\sigma_n$) to understand the evolution of shear velocity. The main experimental results are described in the following.

3.1 Role of Different Normal Stress Reduction Rates

Following the procedures described in Sect. 2.3, the shale gouge was initially sheared at a pre-defined shear velocity until reaching steady-state friction. The shear stress was then held constant, and the normal stress was gradually reduced to observe how fault shear velocity evolves. We first examine the effect of normal stress reduction rate on fault shear velocity evolution (Fig. 6). According to Amontons' law ($\tau=\mu\cdot(\sigma_n-P_f)=\mu\cdot\sigma_{neff}$), increasing the (effective) normal stress reduction rate is equivalent to increasing the rate of elevating the pore fluid pressure. This process represents an increased CO_2 injection rate during geologic storage (Cameron And Durlofsky 2012; Kolster et al. 2018). Shear velocity evolution with increasing time for tests CHS_NR1, CHS_NR2, CHS_NR5, and CHS_NR10 are all similar. All were sheared at an initial shear velocity of 1.0 µm/s with the velocity reduced to 0 µm/s after holding the shear stress constant while gradually reducing the normal stress. Finally, the velocity increased exponentially to the peak shear velocity after nucleation durations of tens to hundreds of seconds.

With an increase in normal stress reduction rate, the duration of nucleation monotonically decreases from > 100 s to < 40 s, while the peak shear velocity monotonically increases from ~ 300 µm/s to ~ 2400 µm/s (Figs. 7 and 8

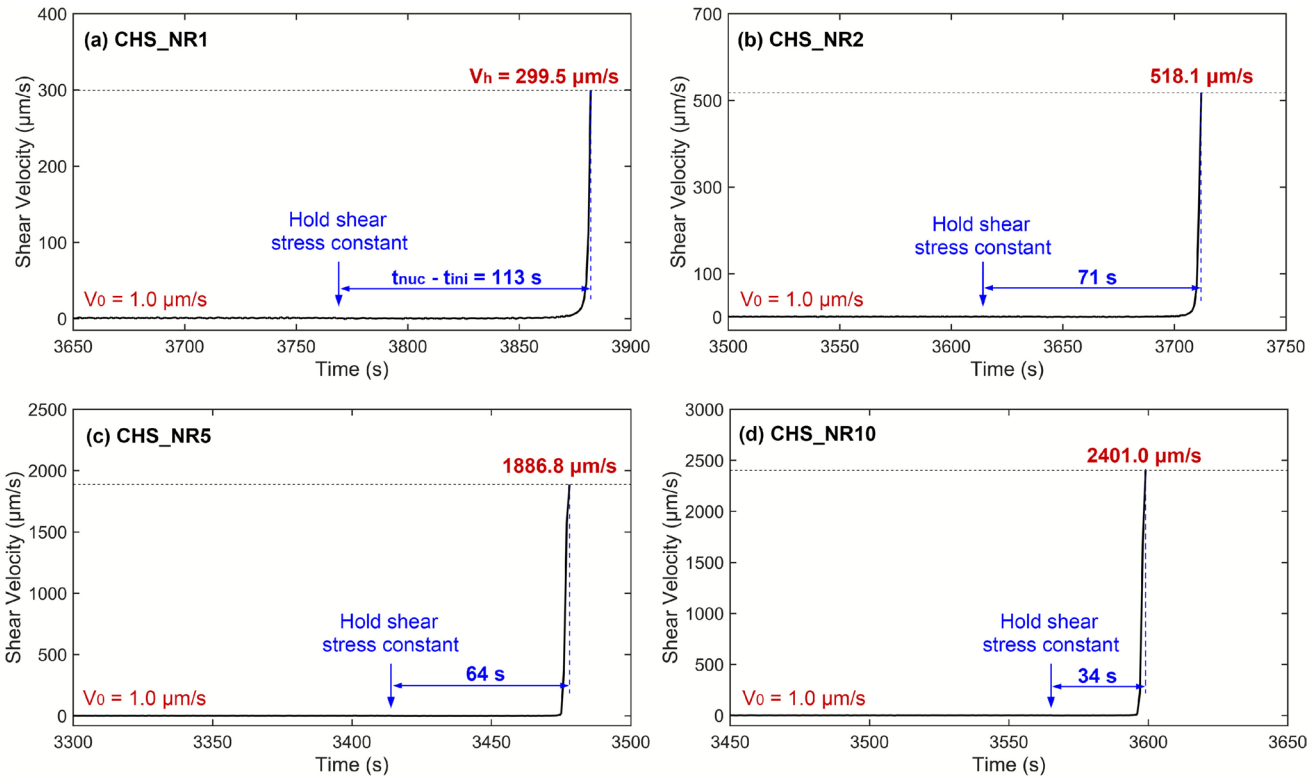

Fig. 6 Shear velocity evolution with increasing time at different normal stress reduction rates, **a** CHS_NR1, **b** CHS_NR2, **c** CHS_NR5, and **d** CHS_NR10. Blue arrows indicate the duration of holding the shear stress constant

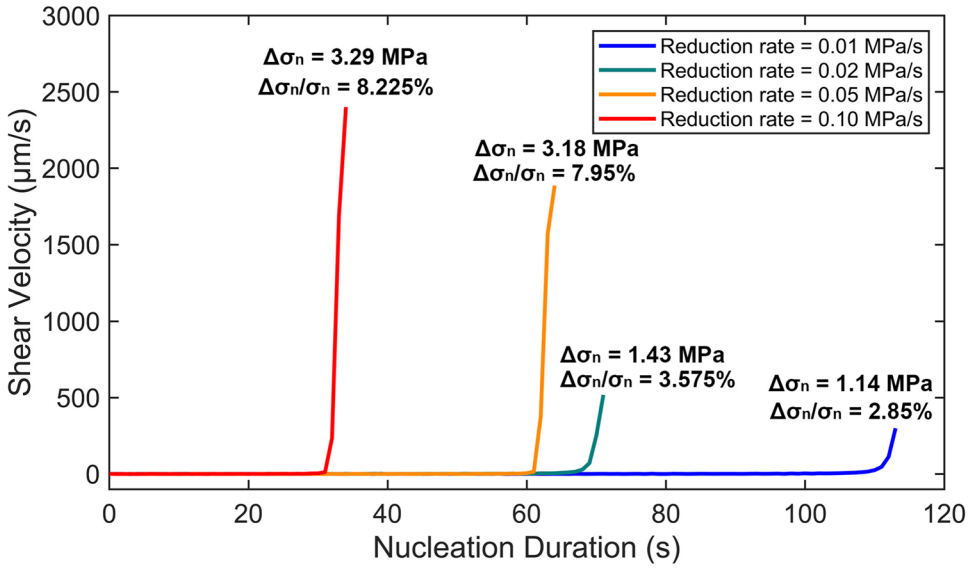

Fig. 7 Shear evolution at different normal stress reduction rates. Values of the normal stress drop ($\Delta\sigma_n$) and the ratios of normal stress drop to initial normal stress ($\Delta\sigma_n/\sigma_n$) are added to the figure. The normal stress drop indicates the normal stress change from holding the shear stress constant to reaching the maximum shear velocity

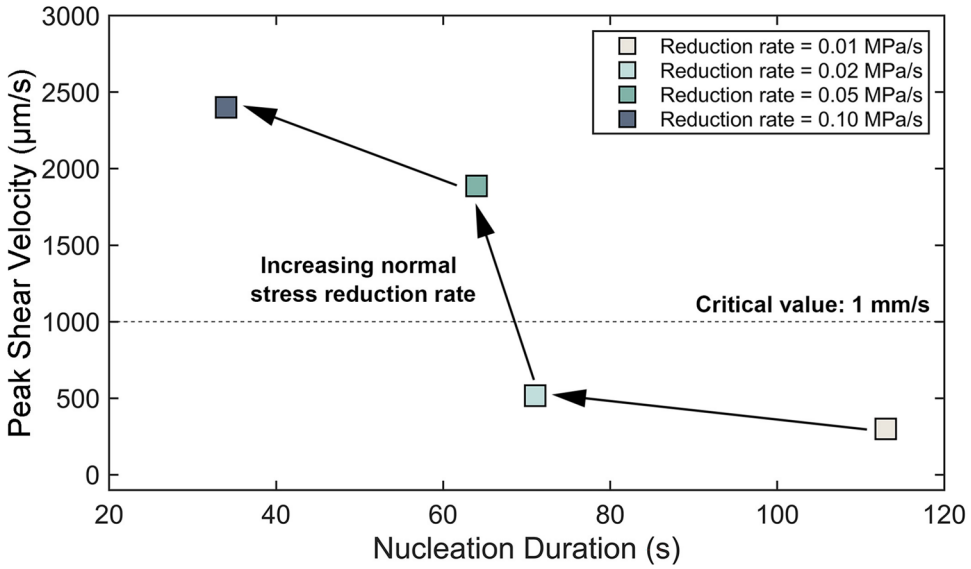

Fig. 8 Relationship between peak shear velocity and nucleation duration at different normal stress reduction rates. The dashed line indicates a critical dynamic fault slip rate of 1 mm/s for earthquake triggering

and S1 in the supporting information). The largest increase in maximum shear velocity occurs when the normal stress reduction rate is elevated from 0.02 to 0.05 MPa/s. The peak shear velocities at normal stress reduction rates of 0.05 (V_h = 1886.8 μm/s) and 0.10 MPa/s (V_h = 2401.0 μm/s) all exceed dynamic fault slip rates (~ mm/s), implying the possibility of triggering seismicity (Fig. 8). Meanwhile, the stress drops ($\Delta\sigma_n$) during the nucleation process are also correlated with the normal stress reduction rates, and both $\Delta\sigma_n$ and $\Delta\sigma_n/\sigma_n$ values are positively correlated to the normal stress reduction rate (Fig. 7). The values of $\Delta\sigma_n/\sigma_n$ approach ~ 8% at normal stress reduction rates of 0.05 and 0.10 MPa/s, but they reduce to ~ 3% at normal stress reduction rates of 0.01 and 0.02 MPa/s. These results document that increasing the normal stress reduction rate could lower the duration of nucleation and elevate the maximum shear velocity and normal stress drop, demonstrating the direct destabilizing effect of elevating equivalent pore fluid pressures.

3.2 Role of Varied Initial Normal Stresses and Shear Velocities

Magnitudes of applied normal stress reflect varied tectonic stress conditions and reservoir depths. The burial depths of Longmaxi shales are typically within the range of 1.5–3.0 km in the southeastern Sichuan Basin, represented by normal stress in the range of 20 to 60 MPa (An et al. 2020b; Dong et al. 2018), with experimental curves shown in Fig. 9. Shear velocity curves at initial normal stresses of 20–50 MPa are similar, with the shear velocity rapidly

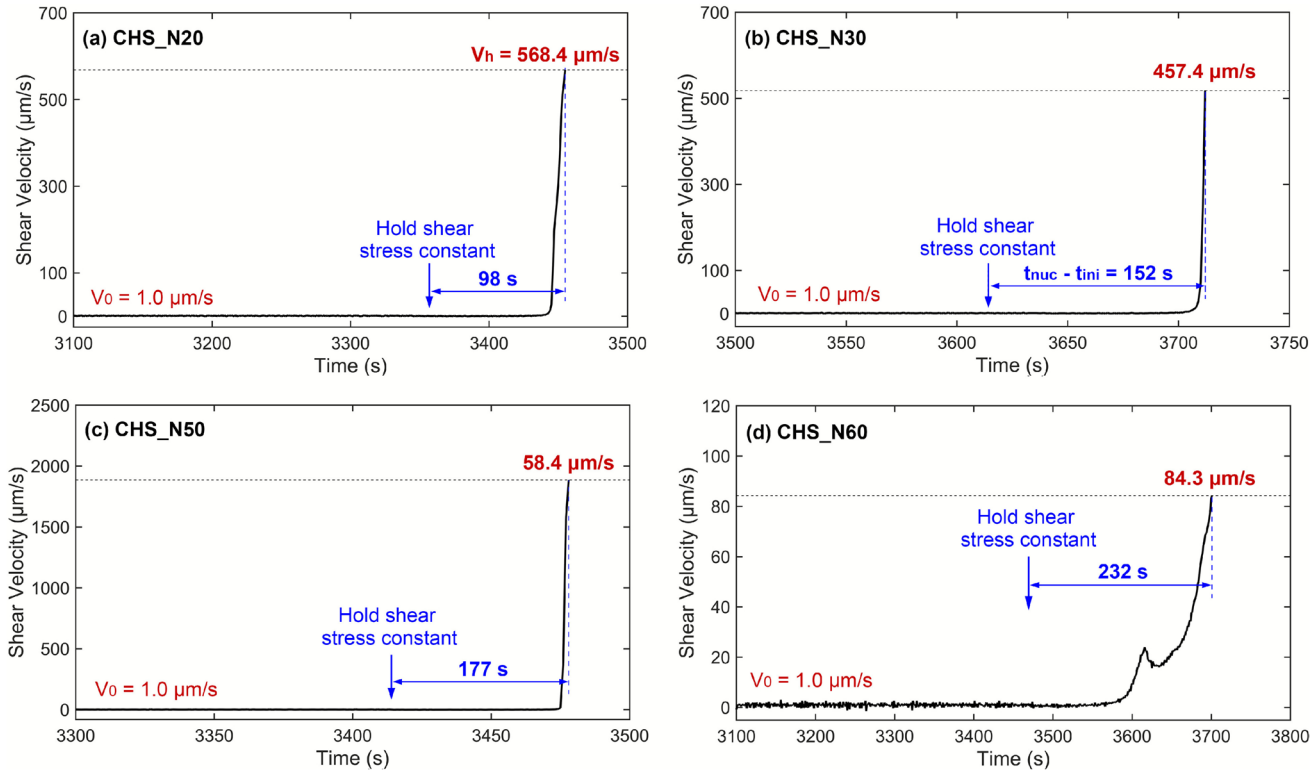

Fig. 9 Shear velocity evolution with increasing time at different initial normal stresses, **a** CHS_N20, **b** CHS_N30, **c** CHS_N50, and **d** CHS_N60. Blue arrows indicate the duration of holding the shear stress constant

evolving from zero to the peak shear velocity after holding the shear stress constant (Figs. 6a and 9a–c). However, the duration of nucleation at $\sigma_n = 60$ MPa is much longer (> 230 s), with the velocity slowly evolving to the peak shear velocity compared to tests at lower normal stresses. With an increase in fault initial normal stress, the peak shear velocity gradually decreases from > 550 to < 100 μm/s, and the duration of nucleation increases from ~ 100 s to > 230 s (Figs. 10 and 11 and S2). Similar to the results in Sect. 3.1, the fault peak shear velocity decreases with increasing nucleation durations at higher initial normal stresses. However, the peak shear velocity at initial normal stresses of 20–60 MPa

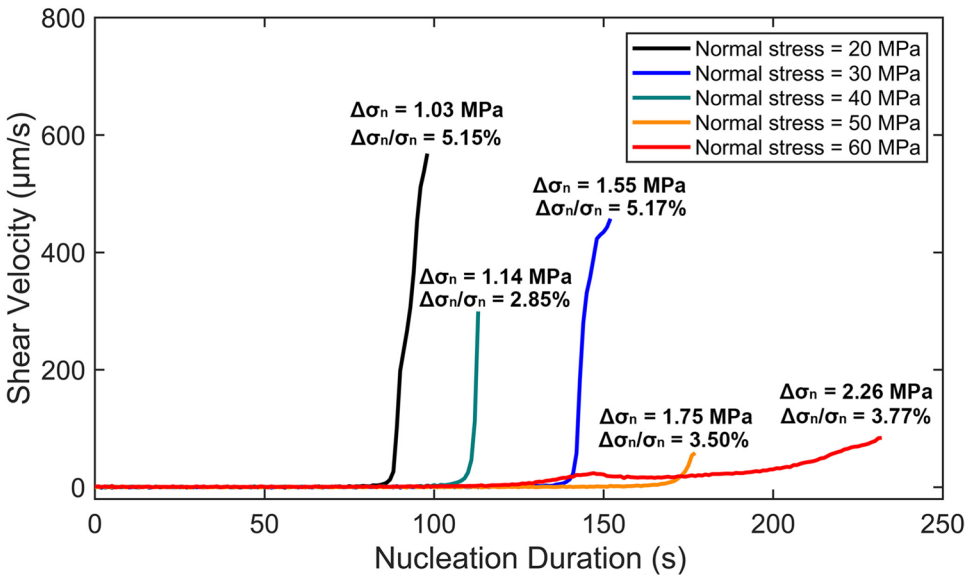

Fig. 10 Fault shear evolution at different initial normal stresses, with values of $\Delta\sigma_n$ and $\Delta\sigma_n/\sigma_n$ marked

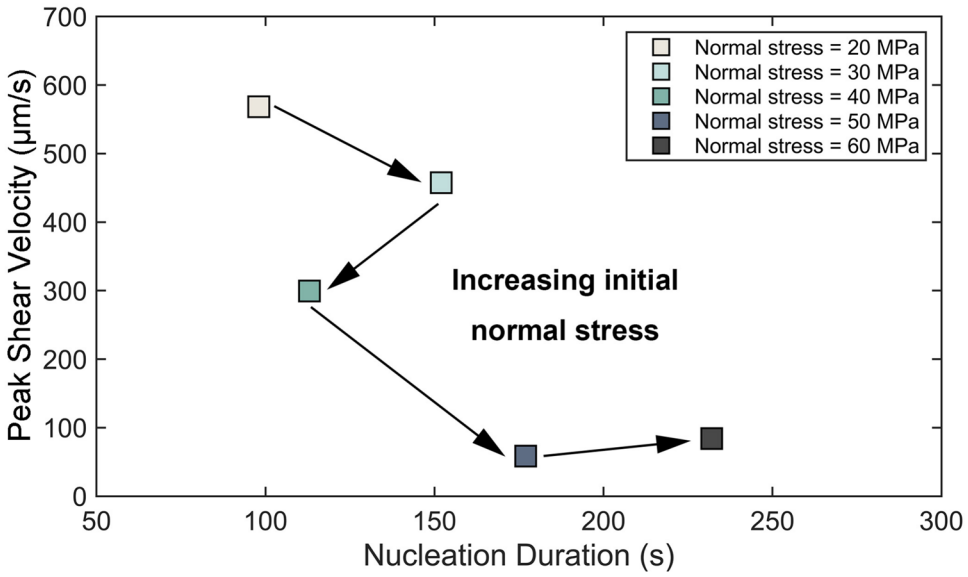

Fig. 11 Variation in maximum shear velocity with the nucleation duration for different initial normal stresses

are all below the dynamic fault slip rate (~ mm/s), indicating the reduced possibility of triggering seismicity by pressure perturbation (Fig. 11). Values of $\Delta\sigma_n$ at different initial normal stresses are low, and all < 2.5 MPa (Fig. 10). Values of $\Delta\sigma_n/\sigma_n$ at σ_n = 20–30 MPa are high and approach 5%, but reduce to ~ 3–3.5% for σ_n = 40–60 MPa (Fig. 10). These data show that increasing the initial normal stress evidently lowers the peak shear velocity and $\Delta\sigma_n/\sigma_n$ but extends the duration of nucleation, identifying a propensity for destabilization at lower effective pressures.

We shear the gouge at a pre-defined velocity for a shear displacement of 2–3 mm before simulating the nucleation process. This replicates the slip behavior of natural faults as natural faults are primarily in a stable (steady) state before CO_2 injection. Pre-slip was applied to ensure steady state of friction (Savage And Marone 2007). As dictated by our shear apparatus, we could only apply shear velocities of 0.3 to 30 μm/s to maintain steady experimental control (Fig. 12). A shear velocity of 30 μm/s is the highest shear velocity feasible in the apparatus to maintain steady experimental control. At initial shear velocities of 20 and 30 μm/s, the shear velocities evolve more slowly to the peak values than in other cases. When the initial shear velocity was elevated from 0.3 to 10 μm/s, the shale fault peak shear velocity increased from ~ 180 to ~ 820 μm/s, and the duration of nucleation also increased from ~ 130 to ~ 280 s (Fig. S3). This phenomenon differs from increasing the normal stress reduction rate or initial normal stress where the peak shear velocity and the nucleation duration are negatively correlated (Figs. 8 and 11). Moreover, when the initial shear velocity was elevated from 10 to 30 μm/s, the peak shear velocity decreased from ~ 820 to ~ 85 μm/s, and the nucleation duration decreased slightly from ~ 280 to ~ 220 s (Fig. S3). Values of $\Delta\sigma_n$ and $\Delta\sigma_n/\sigma_n$ change positively with the nucleation duration, and they are higher at initial shear velocities of 10–30 μm/s, exceeding 2 MPa and 5%, respectively (Fig. 13). These results show that increasing the initial shear velocity increases the peak shear velocity, nucleation duration and $\Delta\sigma_n$ when the initial shear velocity is below a threshold of 10 μm/s for the current study. In addition to the impact of initial shear velocity, the critical shear velocity (~ 10 μm/s) affects peak shear velocity and the duration of nucleation (see Fig. S3). It is apparent that the high and low initial shear velocities would produce different shale gouge porosities and furthermore impact the fault nucleation process.

3.3 Role of Different Gouge Mineralogies

Shale mineralogy is one of the most important intrinsic factors controlling fault frictional stability based on the velocity-stepping friction experiments (Fang et al. 2018; Kohli and Zoback 2013). The depositional environments of the Longmaxi formation shales undergo a change from intra-shelf to shallow-shelf from the top to the base of the formation, and this depositional setting leads to a strong heterogeneity in Longmaxi shale mineral compositions (Xu et al. 2019; An et al. 2020b). The intra-shelf regions are enriched in siliceous minerals and organic contents due to the abundance of ocean creatures. With a drop in sea level over the shallow shelf, the reduced abundance of ocean creatures result in the decreased contents of siliceous minerals and organics. In addition, abundant carbonate minerals would be deposited on the shallow shelf due to the continental inputs (Xu et al. 2019). Mineral enrichment by ocean fauna ensures a higher proportion of siliceous minerals at the top of the formation, while the continental inputs elevate the carbonaceous contents at the formation base. As noted in many

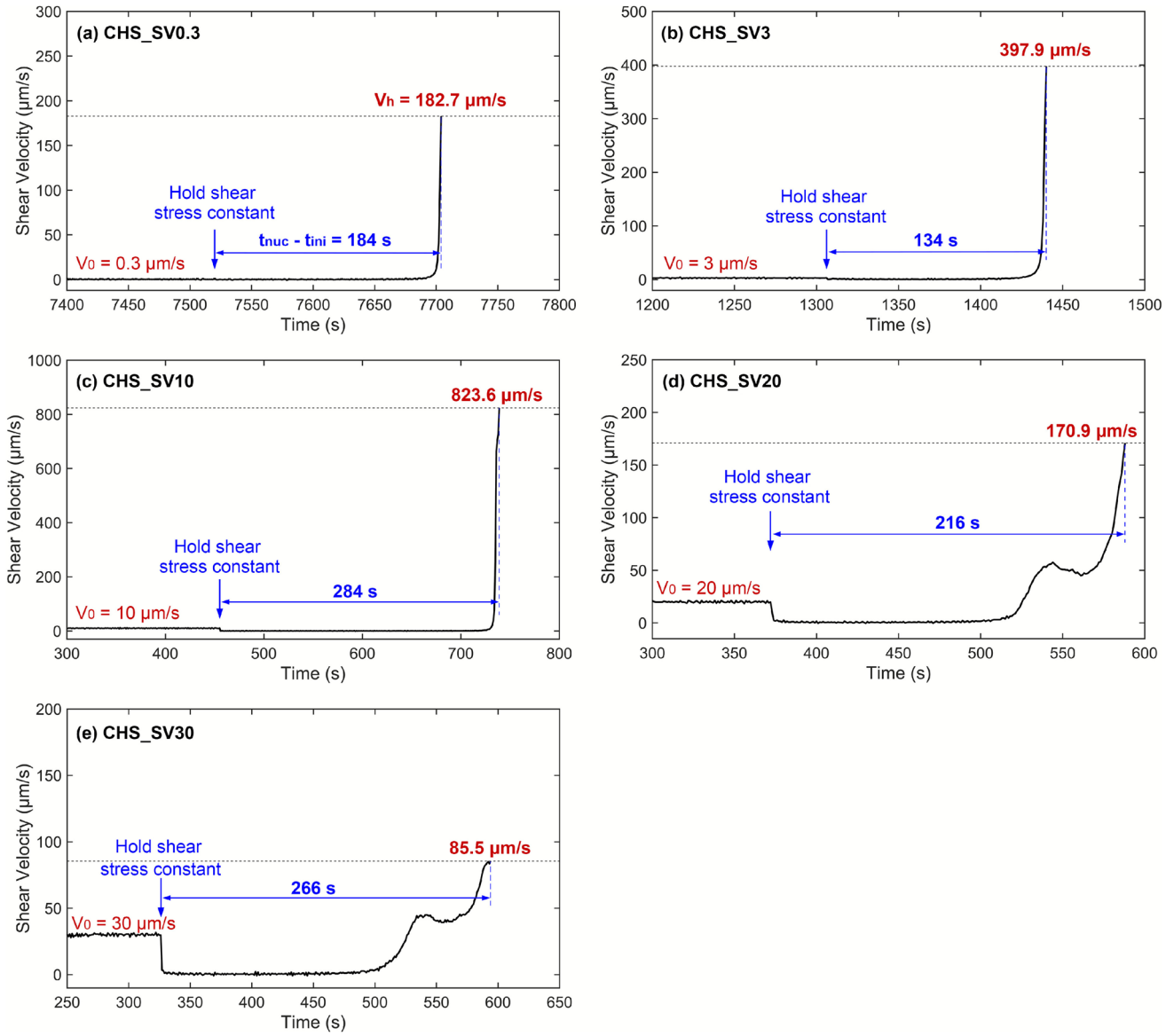

Fig. 12 Shear velocity evolution with increasing time at different initial shear velocities, **a** CHS_SV0.3, **b** CHS_SV3, **c** CHS_SV10, **d** CHS_SV20, and **e** CHS_SV30

previous studies, the phyllosilicate minerals typically show low frictional strength and promote predominantly aseismic fault slip—they are the most important component that controls fault slip evolution and imparts mechanical weakness (Ikari et al. 2009; Carpenter et al. 2011). The tectosilicate and carbonate minerals typically exhibit high frictional strength, and enrichment of these minerals potentially promotes unstable sliding of faults under varied testing conditions (Tembe et al. 2010; Verberne et al. 2015).

Slip reactivation curves of different shale gouges are shown in Fig. 14. The shear velocity evolutions in most shale gouges are similar except for Shale_26 and Shale_35. After holding the shear stress constant, the shear velocities in Shale_26 and Shale_35 first reach a minor peak and then evolve to the highest values. Mineralogy may influence the peak shear velocity and nucleation duration, but the impacts also vary with the proportion of tectosilicates, phyllosilicates and carbonates (Figs. 15, 16 and S4). As tectosilicate content increases, the peak shear velocity increases from ~ 70 to ~ 1760 μm/s, and the nucleation duration increases slightly from ~ 170 to ~ 290 s except for Shale_15 and Shale_29 (Fig. 16a–b). The peak shear velocity apparently decreases with increased carbonate content, and the nucleation duration slightly decreases except for Shale_15 and Shale_29 (Fig. 16c–d). However, there is no evident correlation between the peak shear velocity and nucleation duration

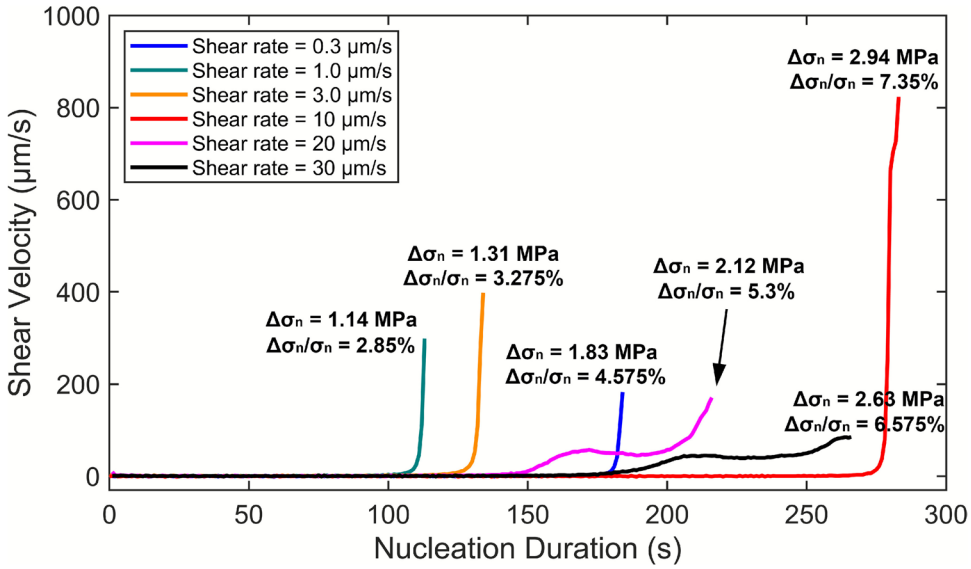

Fig. 13 Shear velocity evolution at different initial shear rates, with values of $\Delta\sigma_n$ and $\Delta\sigma_n/\sigma_n$ marked

with phyllosilicate content (Fig. S4). The lower nucleation durations in Shale_15 and Shale_29 possibly result from the particle sizes and values of D90 in Shale_15 and Shale_29, which are much lower than for other shales (Table 2). In addition, the tectosilicate-rich shale gouges show higher values of $\Delta\sigma_n$ and $\Delta\sigma_n/\sigma_n$ than tectosilicate-lean shale gouges. The values of $\Delta\sigma_n/\sigma_n$ for Shale_7, Shale_11 and Shale_17 all exceed 5.5%. The peak shear velocity for Shale_7 (with the highest tectosilicate content of ~ 76 wt.%) is higher than the dynamic fault slip rate for triggering the seismicity, indicating the higher possibility of tectosilicate-rich faults to promote unstable sliding. As for, for the impact of shale mineralogy, the shale gouge nucleation process is controlled by a combination of the three mineral groups rather than that of a single mineral group—thus the peak shear velocity and duration of nucleation may be not linearly correlated with shale mineralogy.

4 Discussion

After analyzing the impacts of normal stress reduction rates, initial normal stresses and shear velocities, and mineralogy on shale fault shear velocity evolution, we first discuss the similarities and differences of our results to previous studies and then the implications for shale fault stability during CO_2 storage. We employ the test results to interpret possible fault nucleation mechanisms during CO_2 storage within Longmaxi shales.

4.1 Comparisons with Previous Studies

We have explored the effects of normal stress reduction rates, initial normal stresses, initial shear velocity, and mineralogy on the shear evolution of shale faults under fluid pressure perturbations. As restricted by our shear apparatus, we gradually decreased the (effective) normal stress upon reaching steady-state friction to observe the evolution of shear failure as a proxy for directly elevating pore fluid pressure. The shale gauge generally became stable after holding the shear stress constant and gradually decreasing the normal stress. The shear velocity then increases exponentially to the peak value upon reaching the Coulomb failure criterion (Eq. (2)). The values of peak shear velocity (V_h), nucleation duration ($t_{nuc}-t_{ini}$) and normal stress drops ($\Delta\sigma_n$) vary regularly with changes in the testing conditions. We compare our testing results with field and laboratory tests where fluids are actually injected (Guglielmi et al. 2015; Scuderi And Collettini 2018).

A suite of field fluid injection tests was conducted by Guglielmi et al. (2015) on a fault located in an underground research laboratory in southeastern France. The fault has a length of more than 500 m, and the injection was performed at a depth of ~ 280 m within a carbonate formation. A total of 950 L of water was injected at step-increasing rates from < 10 to > 50 L/min to drive an increase in in-situ pressures and reactivate fault shear displacement and velocities. Results demonstrate a negligible fault shear displacement of ~ 0.1 mm within the initial 800 s, to displacements of ~ 0.3 mm at ~ 1100 s and ~ 1.2 mm at ~ 1400 s, accompanied by then exponentially increased fault slip rates from ~ 4 μm/s before 1100 s to ~ 23 μm/s after 1100 s. A congruent laboratory experiment driving fault creep was performed by Scuderi and Collettini (2018) to similarly characterize slip evolution with increasing pore fluid pressures on Rochester shale (68% illite–kaolinite and 27% quartz–plagioclase). The fault was initially sheared at a rate of 10 μm/s until a steady-state friction was achieved,

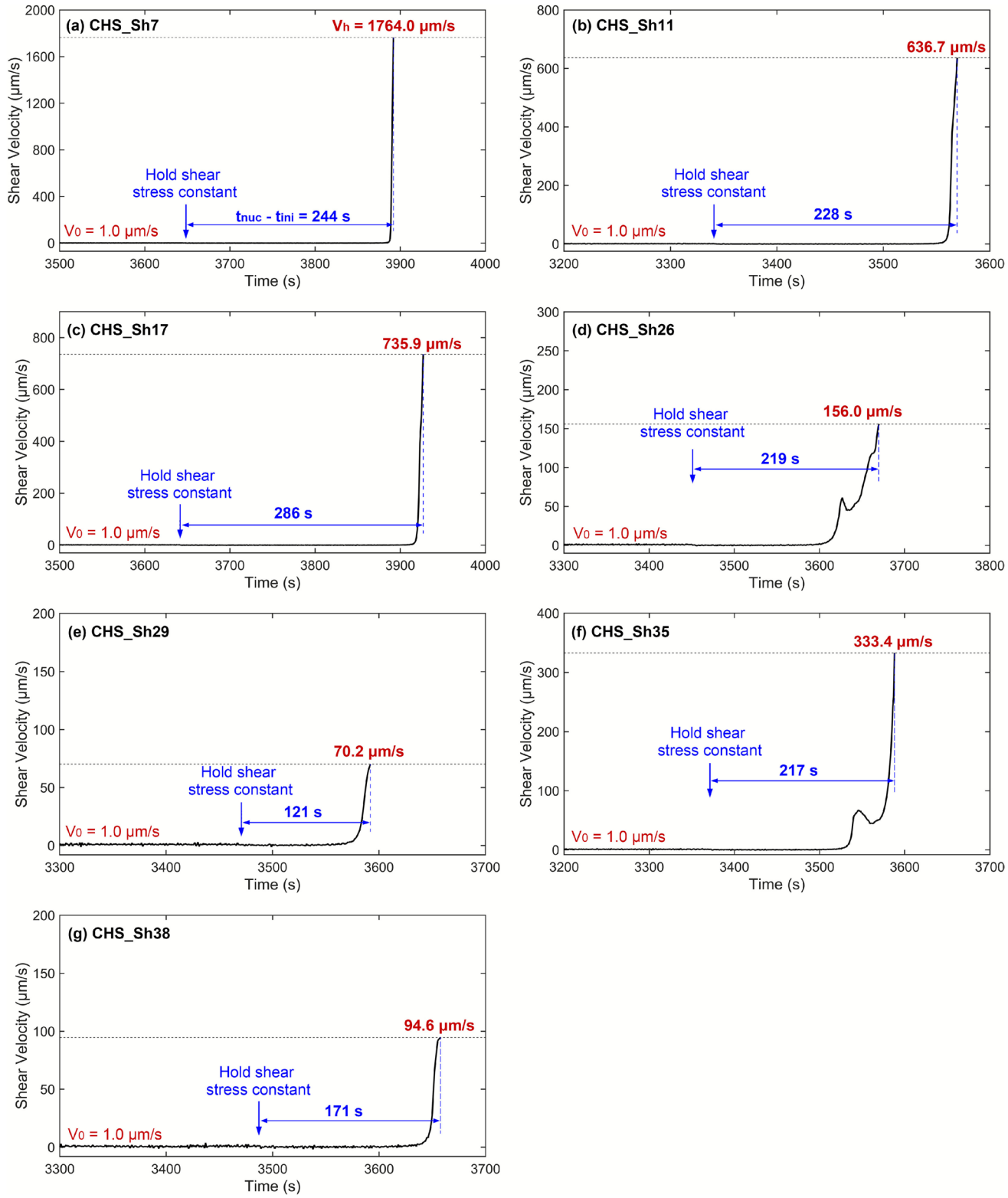

Fig. 14 Shear velocity evolution for different shale gouges, **a** CHS_Sh7, **b** CHS_Sh11, **c** CHS_Sh17, **d** CHS_Sh26, **e** CHS_Sh29, **f** CHS_Sh35, and **g** CHS_Sh38

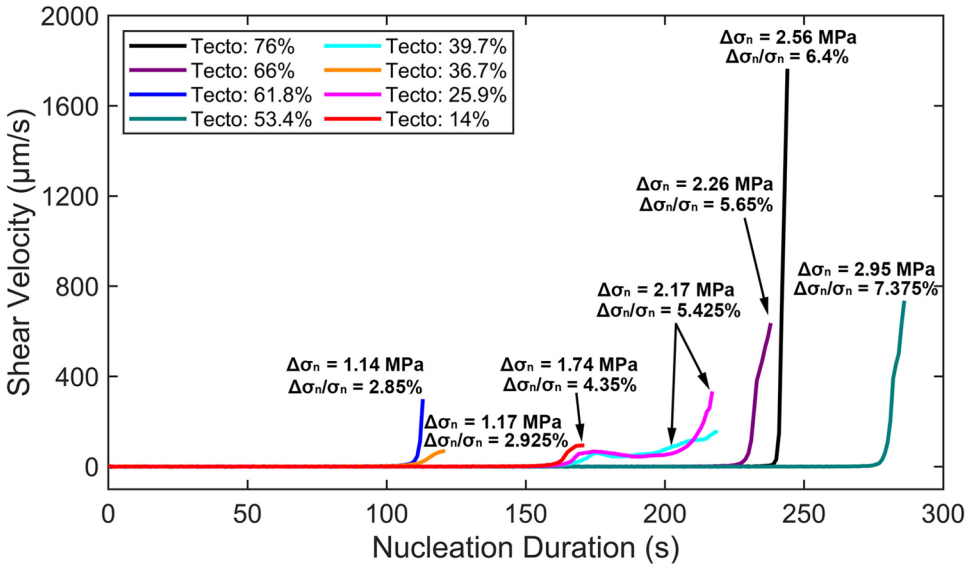

Fig. 15 Shear velocity evolution for different shale gouge materials, with values of $\Delta\sigma_n$ and $\Delta\sigma_n/\sigma_n$ marked. Tecto represents the proportion of tectosilicate minerals

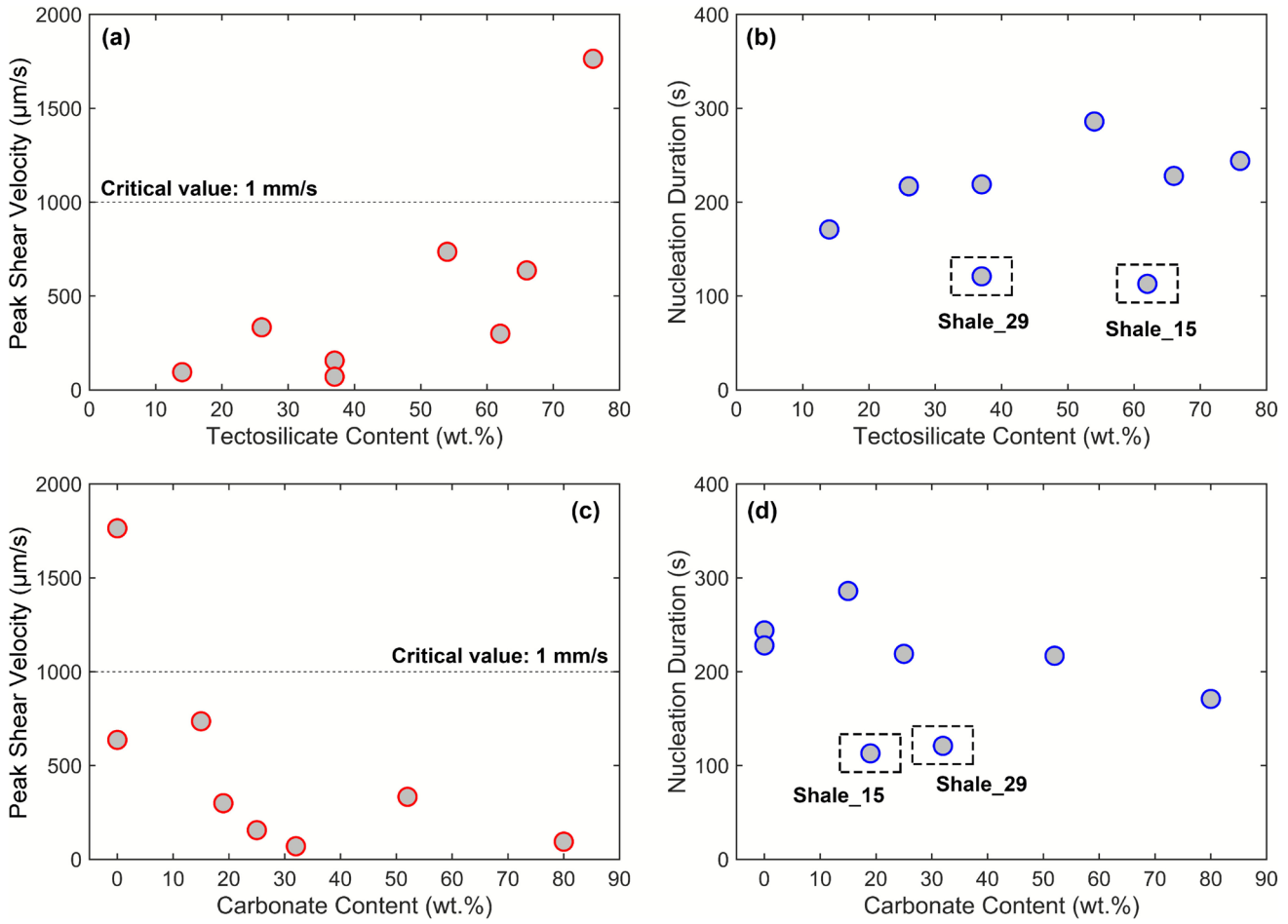

Fig. 16 Peak shear velocity and nucleation duration for different mineral contents. Panels **a**, **b** show the relationships of peak shear velocity and nucleation duration with tectosilicate content, respectively. Panels **c**, **d** show the relationships of peak shear velocity and nucleation duration with carbonate content, respectively

and shearing then stopped to allow the sample to relax to residual shear strength. Next, the feedback control on shear was switched from displacement to load control and set a shear stress of ~ 80/90% of the steady-state shear strength. Finally, the fault was left to creep for an hour before elevating the pore fluid pressure at a pre-defined rate. Results identify a trimodal fault slip behavior upon fluid pressurization, i.e., an initial decelerating creep followed by steady-state creep before the final dynamic slip. However, the failure slip velocity of the Rochester shale gouge remained lower (~ 200 μm/s) than the dynamic slip rate. Our testing results are consistent with the two examples that show an exponentially increased fault slip velocity that could be observed upon fluid pressurization. But our pressure perturbation rate (0.01–0.10 MPa/s) is much higher than that (1 MPa/h or 0.2 MPa/12 min) in Scuderi and Collettini (2018), and the achieved peak shear velocity could exceed the dynamic slip rate (~ mm/s). Although we did not directly elevate the pore fluid pressure but rather adopted an equivalent method to gradually decrease the (effective) normal stress, this method is a convenient way to reflect the shear velocity evolution upon fluid pressurization during CO_2 storage in fractured shale reservoirs.

4.2 Implications for Shale Fault Stability During CO_2 Storage

Using a proxy for fluid pressurization, our results aid in understanding reactivation response during CO_2 storage. Our normal stress reduction rates are 0.01–0.10 MPa/s and much higher than field injection rates that are typically on the order of several hours to days per MPa (Osiptsov 2017). At much lower normal stress reduction rates, the induced peak shear velocity barely approaches the dynamic fault slip rate and directly triggers seismicity (Fig. 7). Reservoirs depths are generally of the order of 1.5–3 km in the southeastern Sichuan Basin with lithostatic pressures > 40 MPa. With increased confined pressures, the induced peak shear velocity would also decrease and below the dynamic fault slip rate (Fig. 10). Although the Longmaxi shales show strong heterogeneity in mineral composition, the Longmaxi shale gouge only develops a peak shear velocity of one tectosilicate-rich shale larger than the dynamic fault slip rate (Fig. 15). Consequently, most shale faults should slide stably upon the fluid pressurization during CO_2 storage.

Another important question is whether faults in Longmaxi shale will exhibit velocity-weakening or velocity-strengthening behavior. Based on rate and state friction, velocity-strengthening faults will only promote aseismic slip, while velocity-weakening faults potentially promote fault unstable sliding when the critical stiffness condition is also met (Dieterich 1979; Ruina 1983; Gu et al. 1984). The frictional stability of Longmaxi shales has been evaluated at a confining pressure of 60 MPa, pore fluid pressure of 30 MPa and temperature of 150 °C by An et al. (2020b). The results indicate that only tectosilicate-rich or carbonate-rich shale gouge exhibits velocity-weakening response and thus may host unstable sliding—these shales only account for 5% of the strata in the Longmaxi formation. Shear velocity evolution, combined with the frictional stability analysis, demonstrates the importance of shale fault aseismic slip in triggering seismicity, similar to that observed in hydraulic fracturing for shale gas exploitation (An et al. 2020b). As a result of the strong heterogeneity in the mineralogy of the Longmaxi shales, only the tectosilicate-rich or carbonate-rich fractures/faults are prone to be seismogenic. CO_2 injection into fractured shale reservoirs would elevate fluid pressures and could induce aseismic fault slip. Poroelastic stress transfer could also conspire to shed loading onto distant seismic-capable faults and trigger seismicity (Fig. 17). This mechanism could provide a possible explanation for the earthquake occurrence during both the CO_2 storage in fractured shale reservoirs and that observed in hydraulic fracturing for shale gas exploitation in the southeastern Sichuan Basin.

We may estimate potential earthquake magnitudes based on the observed normal stress drops in the shear tests. The seismic moment (M_0) may be calculated from the shear stress drop ($\Delta\tau$) values based on Brune's source model for a circular crack (Brune 1970; Vouillamoz et al. 2016) as

$$M_0 = \frac{16}{7} \bullet \Delta\tau \bullet r^3 \tag{3}$$

where r represents the fault radius, and the shear stress drop $\Delta\tau$ is estimated from the normal stress drop ($\Delta\sigma_n$), expressed as

$$\Delta\tau = \mu_L \bullet \Delta\sigma_n \tag{4}$$

where μ_L represents the coefficient of friction of the Longmaxi shale gouges (typically ~ 0.5–0.6 (An et al. 2020b)). The relationship of earthquake moment magnitude (M_w) to seismic moment (M_0) is

$$M_w = \frac{2}{3} \bullet \log M_0 - 6 \tag{5}$$

In the southeastern Sichuan Basin, the lower Silurian Longmaxi shale generally has a thickness of 50–550 m and a burial depth of 1.5–3.0 km. Hence, the lengths of pre-existing faults transecting the shale could be of the order of ~ 10^3 m (Jiang et al. 2016). A normal stress of 40 MPa represents a burial depth of 2.0 km. For a coefficient of friction of 0.6 and normal stress drops within the range 1–3 MPa (Figs. 7, 10, 13 and 15), an earthquake moment magnitude (M_w) induced by the CO_2 storage could reach 0–1, 2–3, and 4–5 for fault radii of ~ 10^1 m, ~ 10^2 m, and ~ 10^3 m,

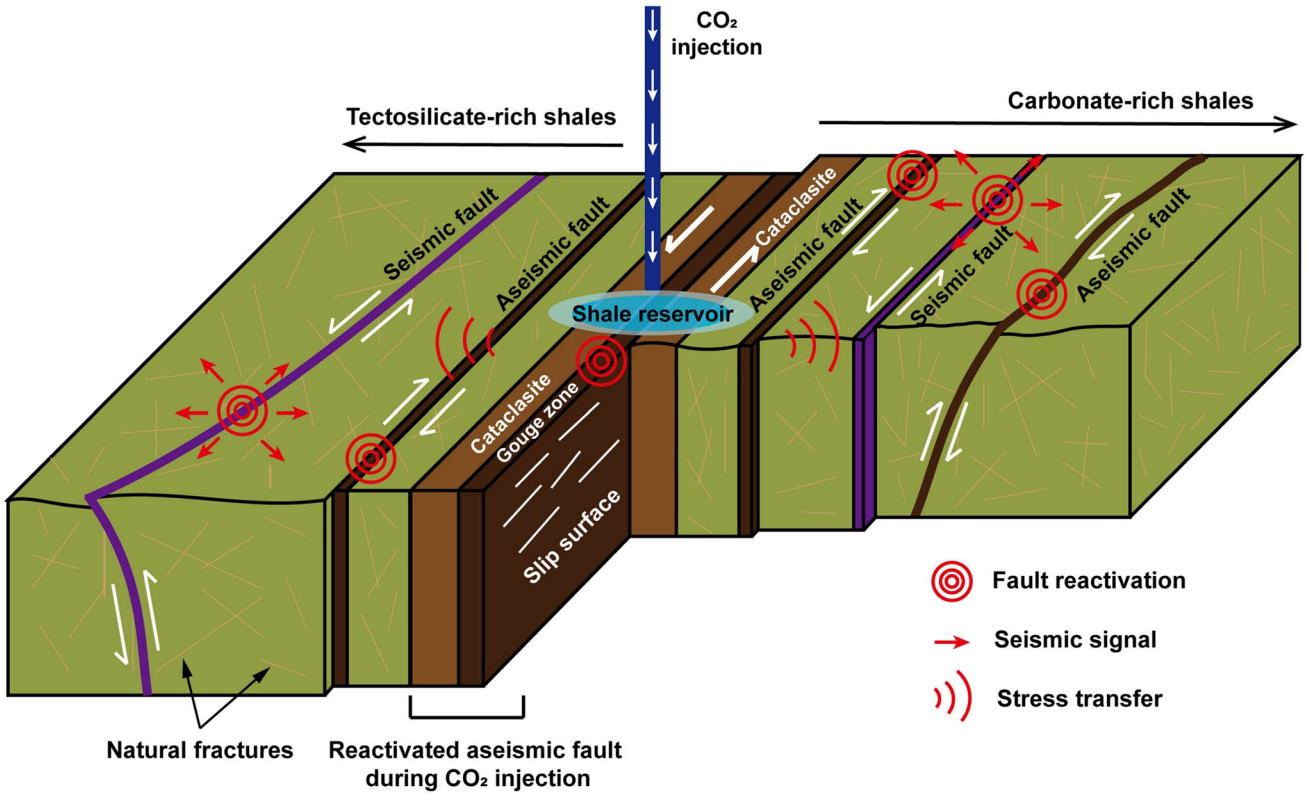

Fig. 17 Schematic showing fault response to CO_2 storage in fractured shale reservoirs (modified from Westaway & Burnside (2019)). Shale fault may be either frictionally stable or unstable due to mineralogic heterogeneity (tectosilicate-rich or carbonate-rich). The blue elliptical area represents the fractured shale reservoir for CO_2 storage. This figure is also based on Longmaxi formation shales to include both the tectosilicate-rich and carbonate-rich shales

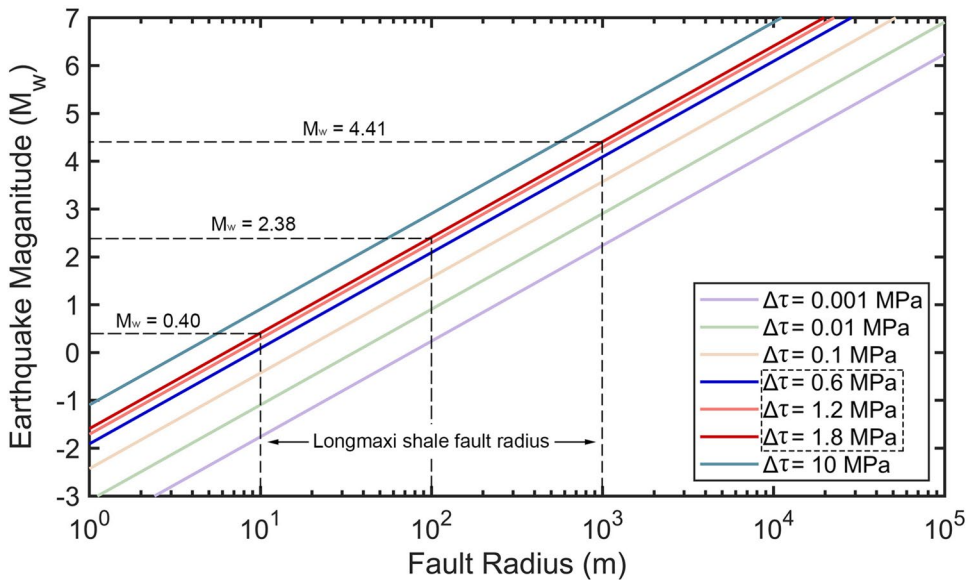

Fig. 18 Relationship among earthquake moment magnitude (M_w), fault radius (r), and shear stress drop ($\Delta\tau$) (modified from Zoback & Gorelick (2012))

respectively (Fig. 18). Currently, earthquake magnitudes (M_L) induced by hydraulic fracturing in the Changning and Weiyuan blocks, southeastern Sichuan Basin are already larger than 4.0 (An et al. 2020b) with this also providing bounds for the possibility of triggering moderate earthquakes during CO_2 injection. Increasing CO_2 injection rates (i.e., the normal stress reduction rates in these experiments) and confining pressures (i.e., the initial normal stresses

representing burial depth) all potentially elevate the magnitude of stress drops and the earthquake moment magnitude (Figs. 7 and 10).

5 Conclusions

We report double-direct shear tests on synthetic Longmaxi shale gouges to define controls of pressure perturbations on the potential for fault reactivation during CO_2 storage in the fractured shale reservoirs of the southeastern Sichuan Basin. We use normal stress perturbations as a proxy for fluid pressurization and assume that the increase in pore fluid pressure is equivalent to the decrease in effective normal stress. During fault shear, we also hold the shear stress constant and regard this point as the start of fault nucleation process. The effects of equivalent pressure reduction rate, magnitudes of initial confined stress and shear velocity, and shale mineralogy are analyzed. The main conclusions are described as follows.

Pressure reduction rate. An increase in stress reduction rate (equivalent to fluid pressure increase rate) reflects the response to CO_2 storage at increased fluid injection rates. Elevating the normal stress reduction rates from 0.01 to 0.10 MPa/s significantly increases peak shear velocity and to higher than the fault dynamic slip rate for earthquake triggering and apparently shortens the duration of nucleation. This demonstrates that the fluid pressure increase rate is an important external factor in earthquake triggering.

Initial confined stress and shear velocity. The magnitude of the initial confining stress represents CO_2 storage at different reservoir depths with varied initial shear velocities producing different fault gouge initial states. Lowering the confining stress from 60 to 20 MPa and the shear velocity from 0.3 to 10 μm/s produces similar effects to elevating the pressure reduction rate.

Shale mineralogy. The proportion of tectosilicates is known to gradually decrease from the top to the base of Longmaxi formation, with carbonate contents exhibiting the opposite trend. Elevating the tectosilicate content leads to increases in both peak shear velocities on the fault and the duration of nucleation. However, increasing carbonate contents shows the opposite trend. Shear slip evolution does not show an obvious variation with the proportion of phyllosilicates.

Implications. Our shear experiments indicate that faults in the Longmaxi shale typically slip at velocities below the dynamic fault slip rate for earthquake triggering. This observed shear velocity evolution, combined with the observed tendency for frictional stability, provides evidence of the importance of aseismic fault slips in triggering seismicity during CO_2 storage in fractured shale reservoirs.

Supplementary Information The online version contains supplementary material available at https://doi.org/10.1007/s00603-025-05157-5.

Acknowledgements This research is funded by the National Natural Science Foundation of China (42107163 & 42374070). DE acknowledges the support from the G. Albert Shoemaker endowment. We appreciate the assistance from Yihui Luo and Long Zhang in conducting the shale fault shear experiments.

Author Contributions Mengke An: Conceptualization, Data Curation, Formal Analysis, Methodology, Writing-Original Draft, Funding Acquisition. Rui Huang: Data Curation, Formal Analysis, Writing-Review & Editing. Zhen-Yu Yin: Data Curation, Formal Analysis, Writing-Review & Editing. Ke Gao: Resources, Data Curation, Writing-Review & Editing, Funding Acquisition. Derek Elsworth: Data Curation, Writing-Review & Editing, Funding Acquisition.

Funding National Natural Science Foundation of China, 42107163, Mengke An, 42374070, Ke Gao, the G. Albert Shoemaker endowment, Derek Elsworth.

Data availability Data are available from the corresponding author on reasonable request.

Declarations

Conflict of interest We declare that we have no known competing financial interests or personal relationships that could have appeared to influence the work reported in this article.

References

Al Hameli F, Belhaj H, Al Dhuhoori M (2022) CO_2 sequestration overview in geological formations: trapping mechanisms matrix assessment. Energies 15(20):7805. https://doi.org/10.3390/en15207805

Alam MM, Hjuler ML, Christensen HF, Fabricius IL (2014) Petrophysical and rock-mechanics effects of CO_2 injection for enhanced oil recovery: experimental study on chalk from South Arne field, North Sea. J Pet Sci Eng 122:468–487. https://doi.org/10.1016/j.petrol.2014.08.008

Ambrose WA, Lakshminarasimhan S, Holtz MH, Núñez-López V, Hovorka SD, Duncan I (2008) Geologic factors controlling CO_2 storage capacity and permanence: case studies based on experience with heterogeneity in oil and gas reservoirs applied to CO_2 storage. Environ Geol 54(8):1619–1633. https://doi.org/10.1007/s00254-007-0940-2

An M, Huang H, Zhang F, Elsworth D (2020a) Effect of slick-water fracturing fluid on the frictional properties of shale reservoir rock gouges. Geomech Geophys Geo-Energy Geo-Resour 6:28. https://doi.org/10.1007/s40948-020-00153-1

An M, Zhang F, Elsworth D, Xu Z, Chen Z, Zhang L (2020b) Friction of Longmaxi shale gouges and implications for seismicity during hydraulic fracturing. J Geophys Res Solid Earth 125:e2020JB019885. https://doi.org/10.1029/2020JB019885

Baabbad HKH, Artun E, Kulga B (2022) Understanding the controlling factors for CO_2 sequestration in depleted shale reservoirs using data analytics and machine learning. ACS Omega 7(24):20845–20859. https://doi.org/10.1021/acsomega.2c01445

Bao X, Eaton DW (2016) Fault activation by hydraulic fracturing in western Canada. Science 354(6318):1406–1409. https://doi.org/10.1126/science.aag2583

Bashir A, Ali M, Patil S, Aljawad MS, Mahmoud M, Al-Shehri D et al (2024) Comprehensive review of CO_2 geological storage: exploring principles, mechanisms, and prospects. Earth-Sci Rev 249:104672. https://doi.org/10.1016/j.earscirev.2023.104672

Boosari SSH, Aybar U, Eshkalak MO (2015) Carbon dioxide storage and sequestration in unconventional shale reservoirs. J Geosci Environ Prot 3(1):7–15. https://doi.org/10.4236/gep.2015.31002

Brune JN (1970) Tectonic stress and the spectra of seismic shear waves from earthquakes. J Geophys Res 75(26):4997–5009. https://doi.org/10.1029/JB075i026p04997

Bui M, Adjiman CS, Bardow A, Anthony EJ, Boston A, Brown S et al (2018) Carbon capture and storage (CCS): the way forward. Energy Environ Sci 11(5):1062–1176. https://doi.org/10.1039/C7EE02342A

Busch A, Alles S, Gensterblum Y, Prinz D, Dewhurst DN, Raven MD et al (2008) Carbon dioxide storage potential of shales. Int J Greenhouse Gas Control 2(3):297–308. https://doi.org/10.1016/j.ijggc.2008.03.003

Cameron DA, Durlofsky LJ (2012) Optimization of well placement, CO_2 injection rates, and brine cycling for geological carbon sequestration. Int J Greenhouse Gas Control 10:100–112. https://doi.org/10.1016/j.ijggc.2012.06.003

Cappa F, Rutqvist J (2011) Modeling of coupled deformation and permeability evolution during fault reactivation induced by deep underground injection of CO_2. Int J Greenhouse Gas Control 5(2):336–346. https://doi.org/10.1016/j.ijggc.2010.08.005

Carpenter BM, Marone C, Saffer DM (2011) Weakness of the San Andreas fault revealed by samples from the active fault zone. Nat Geosci 4(4):251–254. https://doi.org/10.1038/ngeo1089

Chen S, Liu J, Zhang Q, Teng F, McLellan BC (2022) A critical review on deployment planning and risk analysis of carbon capture, utilization, and storage (CCUS) toward carbon neutrality. Renew Sustain Energy Rev 167:112537. https://doi.org/10.1016/j.rser.2022.112537

Dieterich JH (1979) Modeling of rock friction: 1. Experimental results and constitutive equations. J Geophys Res 84(B5):2161. https://doi.org/10.1029/JB084iB05p02161

Dong D, Shi Z, Guan Q, Jiang S, Zhang M, Zhang C et al (2018) Progress, challenges and prospects of shale gas exploration in the Wufeng-Longmaxi reservoirs in the Sichuan Basin. Nat Gas Ind B 5(5):415–424. https://doi.org/10.1016/j.ngib.2018.04.011

Edwards RWJ, Celia MA, Bandilla KW, Doster F, Kanno CM (2015) A model to estimate carbon dioxide injectivity and storage capacity for geological sequestration in shale gas wells. Environ Sci Technol 49(15):9222–9229. https://doi.org/10.1021/acs.est.5b01982

Ellsworth WL, Townend J, Zoback MD, Evans KF, Zappone A, Kraft T et al (2013) Injection-induced earthquakes. Science 341:1225942. https://doi.org/10.1126/science.1225942

Elsworth D, Spiers CJ, Niemeijer AR (2016) Understanding induced seismicity. Science 354(6318):1380–1381. https://doi.org/10.1126/science.aal2584

Eshkalak MO, Al-Shalabi EW, Sanaei A, Aybar U, Sepehrnoori K (2014) Simulation study on the CO_2-driven enhanced gas recovery with sequestration versus the refracturing treatment of horizontal wells in the U.S. unconventional shale reservoirs. J Nat Gas Sci Eng 21:1015–1024. https://doi.org/10.1016/j.jngse.2014.10.013

Eyre TS, Eaton DW, Garagash DI, Zecevic M, Venieri M, Weir R et al (2019) The role of aseismic slip in hydraulic fracturing-induced seismicity. Sci Adv 5:eaav7172. https://doi.org/10.1126/sciadv.aav7172

Fang Y, Elsworth D, Wang C, Jia Y (2018) Mineralogical controls on frictional strength, stability, and shear permeability evolution of fractures. J Geophys Res Solid Earth 123:3549–3563. https://doi.org/10.1029/2017JB015338

Faulkner DR, Mitchell TM, Healy D, Heap MJ (2006) Slip on 'weak' faults by the rotation of regional stress in the fracture damage zone. Nature 444:922–925. https://doi.org/10.1038/nature05353

Foulger GR, Wilson MP, Gluyas JG, Julian BR, Davies RJ (2018) Global review of human-induced earthquakes. Earth-Sci Rev 178:438–514. https://doi.org/10.1016/j.earscirev.2017.07.008

Frohlich C, DeShon H, Stump B, Hayward C, Hornbach M, Walter JI (2016) A historical review of induced earthquakes in Texas. Seismol Res Lett 87(4):1022–1038. https://doi.org/10.1785/0220160016

Frye KM, Marone C (2002) Effect of humidity on granular friction at room temperature. J Geophys Res 107(B11):2309. https://doi.org/10.1029/2001JB000654

Fukushima R, Kano K, Hirahara K (2023) Physics-informed neural networks for fault slip monitoring: simulation, frictional parameter estimation, and prediction on slow slip events in a spring-slider system. J Geophys Res Solid Earth 128(12):e2023JB027384. https://doi.org/10.1029/2023JB027384

Furukawa H, Yaghi OM (2009) Storage of hydrogen, methane, and carbon dioxide in highly porous covalent organic frameworks for clean energy applications. J Am Chem Soc 131(25):8875–8883. https://doi.org/10.1021/ja9015765

Gale JFW, Laubach SE, Olson JE, Eichhubl P, Fall A (2014) Natural fractures in shale: a review and new observations. AAPG Bull 98(11):2165–2216. https://doi.org/10.1306/08121413151

Gan Q, Candela T, Wassing B, Wasch L, Liu J, Elsworth D (2021) The use of supercritical CO_2 in deep geothermal reservoirs as a working fluid: insights from coupled THMC modeling. Int J Rock Mech Min Sci 147:104872. https://doi.org/10.1016/j.ijrmms.2021.104872

Gu J-C, Rice JR, Ruina AL, Tse ST (1984) Slip motion and stability of a single degree of freedom elastic system with rate and state dependent friction. J Mech Phys Solids 32(3):167–196. https://doi.org/10.1016/0022-5096(84)90007-3

Guglielmi Y, Cappa F, Avouac J-P, Henry P, Elsworth D (2015) Seismicity triggered by fluid injection-induced aseismic slip. Science 348(6240):1224–1226. https://doi.org/10.1126/science.aab0476

Guo T (2013) Evaluation of highly thermally mature shale-gas reservoirs in complex structural parts of the Sichuan Basin. J Earth Sci 24(6):863–873. https://doi.org/10.1007/s12583-013-0384-4

Han L, Shi X, Ni H, Zhang W, Gao Q (2024) Review of CO_2 fracturing and carbon storage in shale reservoirs. Energy Fuels 38(17):15913–15934. https://doi.org/10.1021/acs.energyfuels.4c01887

Henninges J, Liebscher A, Bannach A, Brandt W, Hurter S, Köhler S et al (2011) PT-β and two-phase fluid conditions with inverted density profile in observation wells at the CO_2 storage site at Ketzin (Germany). Energy Procedia 4:6085–6090. https://doi.org/10.1016/j.egypro.2011.02.614

Hill DP (2008) Dynamic stresses, Coulomb failure, and remote triggering. Bull Seismol Soc Am 98(1):66–92. https://doi.org/10.1785/0120070049

Hou L, Elsworth D, Wang J, Zhou J, Zhang F (2024) Feasibility and prospects of symbiotic storage of CO_2 and H_2 in shale reservoirs. Renew Sustain Energy Rev 189:113878. https://doi.org/10.1016/j.rser.2023.113878

Ikari MJ, Saffer DM, Marone C (2009) Frictional and hydrologic properties of clay-rich fault gouge. J Geophys Res 114:B05409. https://doi.org/10.1029/2008JB006089

Jeanne P, Rutqvist J, Dobson PF, Walters M, Hartline C, Garcia J (2014) The impacts of mechanical stress transfers caused by hydromechanical and thermal processes on fault stability during hydraulic stimulation in a deep geothermal reservoir. Int J Rock Mech Min Sci 72:149–163. https://doi.org/10.1016/j.ijrmms.2014.09.005

Jiang S, Xu Z, Feng Y, Zhang J, Cai D, Chen L et al (2016) Geologic characteristics of hydrocarbon-bearing marine, transitional and lacustrine shales in China. J Asian Earth Sci 115:404–418. https://doi.org/10.1016/j.jseaes.2015.10.016

King GCP, Stein RS, Lin J (1994) Static stress changes and the triggering of earthquakes. Bull Seismol Soc Am 84(3):935–953. https://doi.org/10.1785/BSSA0840030935

Kohli AH, Zoback MD (2013) Frictional properties of shale reservoir rocks. J Geophys Res Solid Earth 118:5109–5125. https://doi.org/10.1002/jgrb.50346

Kolster C, Agada S, Dowell NM, Krevor S (2018) The impact of time-varying CO_2 injection rate on large scale storage in the UK Bunter Sandstone. Int J Greenhouse Gas Control 68:77–85. https://doi.org/10.1016/j.ijggc.2017.10.011

Kuang N, Zhou J, Xian X, Zhang C, Yang K, Dong Z (2023) Geomechanical risk and mechanism analysis of CO_2 sequestration in unconventional coal seams and shale gas reservoirs. Rock Mech Bull 2(4):100079. https://doi.org/10.1016/j.rockmb.2023.100079

Loucks RG, Reed RM, Ruppel SC, Hammes U (2012) Spectrum of pore types and networks in mudrocks and a descriptive classification for matrix-related mudrock pores. AAPG Bull 96(6):1071–1098. https://doi.org/10.1306/08171111061

Louk K, Ripepi N, Luxbacher K, Gilliland E, Tang X, Keles C et al (2017) Monitoring CO_2 storage and enhanced gas recovery in unconventional shale reservoirs: results from the Morgan County, Tennessee injection test. J Nat Gas Sci Eng 45:11–25. https://doi.org/10.1016/j.jngse.2017.03.025

Mair K, Marone C (1999) Friction of simulated fault gouge for a wide range of velocities and normal stresses. J Geophys Res Solid Earth 104(B12):28899–28914. https://doi.org/10.1029/1999JB900279

Matter JM, Broecker WS, Stute M, Gislason SR, Oelkers EH, Stefánsson A et al (2009) Permanent carbon dioxide storage into basalt: the CarbFix pilot project, Iceland. Energy Proc 1(1):3641–3646. https://doi.org/10.1016/j.egypro.2009.02.160

Moein MJA, Langenbruch C, Schultz R, Grigoli F, Ellsworth WL, Wang R et al (2023) The physical mechanisms of induced earthquakes. Nat Rev Earth Environ 4:847–863. https://doi.org/10.1038/s43017-023-00497-8

Mohagheghian E, Hassanzadeh H, Chen Z (2019) CO_2 sequestration coupled with enhanced gas recovery in shale gas reservoirs. J CO2 Util 34:646–655. https://doi.org/10.1016/j.jcou.2019.08.016

Nelson PH (2009) Pore-throat sizes in sandstones, tight sandstones, and shales. AAPG Bull 93(3):329–340. https://doi.org/10.1306/10240808059

Osiptsov AA (2017) Fluid mechanics of hydraulic fracturing: a review. J Pet Sci Eng 156:513–535. https://doi.org/10.1016/j.petrol.2017.05.019

Pan P, Wu Z, Feng X, Yan F (2016) Geomechanical modeling of CO_2 geological storage: a review. J Rock Mech Geotech Eng 8(6):936–947. https://doi.org/10.1016/j.jrmge.2016.10.002

Rogelj J, Schaeffer M, Meinshausen M, Knutti R, Alcamo J, Riahi K et al (2015) Zero emission targets as long-term global goals for climate protection. Environ Res Lett 10(10):105007. https://doi.org/10.1088/1748-9326/10/10/105007

Ruina A (1983) Slip instability and state variable friction laws. J Geophys Res Solid Earth 88(B12):10359–10370. https://doi.org/10.1029/JB088iB12p10359

Savage HM, Marone C (2007) Effects of shear velocity oscillations on stick-slip behavior in laboratory experiments. J Geophys Res Solid Earth. https://doi.org/10.1029/2005JB004238

Scuderi MM, Collettini C (2018) Fluid injection and the mechanics of frictional stability of shale-bearing faults. J Geophys Res Solid Earth 123:8364–8384. https://doi.org/10.1029/2018JB016084

Segall P, Lu S (2015) Injection-induced seismicity: poroelastic and earthquake nucleation effects. J Geophys Res Solid Earth 120(7):5082–5103. https://doi.org/10.1002/2015JB012060

Tan J, Horsfield B, Fink R, Krooss B, Schulz HM, Rybacki E et al (2014) Shale gas potential of the major marine shale formations in the upper Yangtze platform, South China, part III: mineralogical, lithofacial, petrophysical, and rock mechanical properties. Energy Fuels 28(4):2322–2342. https://doi.org/10.1021/ef4022703

Tembe S, Lockner DA, Wong T-F (2010) Effect of clay content and mineralogy on frictional sliding behavior of simulated gouges: binary and ternary mixtures of quartz, illite, and montmorillonite. J Geophys Res 115:B03416. https://doi.org/10.1029/2009JB006383

Verberne BA, Niemeijer AR, De Bresser JHP, Spiers CJ (2015) Mechanical behavior and microstructure of simulated calcite fault gouge sheared at 20–600 °C: implications for natural faults in limestones. J Geophys Res Solid Earth 120:8169–8196. https://doi.org/10.1002/2015JB012292

Vilarrasa V, Carrera J, Bolster D, Dentz M (2013) Semianalytical solution for CO_2 plume shape and pressure evolution during CO_2 injection in deep saline formations. Transp Porous Media 97:43–65. https://doi.org/10.1007/s11242-012-0109-7

Vilarrasa V, Makhnenko R, Gheibi S (2016) Geomechanical analysis of the influence of CO_2 injection location on fault stability. J Rock Mech Geotech Eng 8(6):805–818. https://doi.org/10.1016/j.jrmge.2016.06.006

Vilarrasa V, Carrera J, Olivella S, Rutqvist J, Laloui L (2019) Induced seismicity in geologic carbon storage. Solid Earth 10(3):871–892. https://doi.org/10.5194/se-10-871-2019

Vouillamoz N, Wust Bloch GH, Abednego M, Mosar J (2016) Optimizing event detection and location in low-seismicity zones: case study from Western Switzerland. Bull Seismol Soc Am 106(5):2023–2036. https://doi.org/10.1785/0120160029

Wang H, Chen L, Qu Z, Yin Y, Kang Q, Yu B et al (2020) Modeling of multi-scale transport phenomena in shale gas production — a critical review. Appl Energy 262:114575. https://doi.org/10.1016/j.apenergy.2020.114575

Westaway R, Burnside NM (2019) Fault "corrosion" by fluid Injection: a potential cause of the November 2017 5.5 Korean earthquake. Geofluids. https://doi.org/10.1155/2019/1280721

Xu Z, Jiang S, Yao G, Liang X, Xiong S (2019) Tectonic and depositional setting of the Lower Cambrian and Lower Silurian marine shales in the Yangtze Platform, South China: implications for shale gas exploration and production. J Asian Earth Sci 170:1–19. https://doi.org/10.1016/j.jseaes.2018.10.023

Yin Y, Zhang L, Wang H, Gan M, Wang, Y, Liu, T (2025) Recent progress in CO_2 mineralization to mitigate CO_2 emissions: a review. GeoStorage 1(2):91–112. https://doi.org/10.46690/gs.2025.02.01

Yoshida S, Kato N (2003) Episodic aseismic slip in a two-degree-of-freedom block-spring model. Geophys Res Lett 30(13):1681. https://doi.org/10.1029/2003GL017439

Zhang Z, Tang J, Zhang J, Meng S, Li J (2024) Modeling of scale-dependent perforation geometrical fracture growth in naturally layered media. Eng Geo 336:107499. https://doi.org/10.1016/j.enggeo.2024.107499

Zhang Z, Wang T, Blunt MJ, Anthony EJ, Park AA, Hughes RW et al (2020) Advances in carbon capture, utilization and storage. Appl Energy 278:115627. https://doi.org/10.1016/j.apenergy.2020.115627

Zivar D, Kumar S, Foroozesh J (2021) Underground hydrogen storage: a comprehensive review. Int J Hydrogen Energy 46(45):23436–23462. https://doi.org/10.1016/j.ijhydene.2020.08.138

Zoback MD (2007) Reservoir geomechanics. Cambridge University Press, Cambridge

Zoback MD, Gorelick SM (2012) Earthquake triggering and large-scale geologic storage of carbon dioxide. Proc Natl Acad Sci USA 109(26):10164–10168. https://doi.org/10.1073/pnas.1202473109